International Journal of Fatigue 179 (2024) 108055

Contents lists available at ScienceDirect

International Journal of Fatigue

journal homepage: www.elsevier.com/locate/ijfatigue

Modeling of functional fatigue of SMA-based actuators under thermomechanical loading and Joule heating

Marcos Lopes Leal Júnior [a,b,c,*], Laurent Pino [a], Mahmoud Barati [b,c,d], Luc Saint-Sulpice [a], Laurent Daniel [b,c], Shabnam Arbab Chirani [a]

[a] ENI Brest, UMR CNRS 6027, IRDL, F-29200, Brest, France
[b] Université Paris-Saclay, CentraleSupélec, CNRS, Laboratoire de Génie Électrique et Électronique de Paris, 91192, Gif-sur-Yvette, France
[c] Sorbonne Université, CNRS, Laboratoire de Génie Électrique et Électronique de Paris, 75252, Paris, France
[d] Institut Polytechnique des Sciences Avancées, IPSA, 94200, Ivry-sur-Seine, France

ARTICLE INFO

Keywords:
Shape memory alloys
Thermomechanical coupling
Functional fatigue
Electric activation
Residual strain
Macroscopic model

ABSTRACT

A new constitutive modeling is proposed to simulate the cyclic thermomechanical behavior of SMA-based actuators activated by Joule heating. It uses a weak coupling method to contemplate together the impact of different phenomena highlighted during experimental tests: thermal exchange through the SMA component and with the surrounding, heating by electric current (Joule effect), microstructural evolution leading to performance degradation (functional fatigue), and thermomechanical coupling. After experimental characterization and model implementation, simulation results are compared with experimental tests to validate the strategy and demonstrate its utility for designing SMA-based actuators.

1. Introduction

Shape Memory Alloys (SMAs) are a good illustration of a smart materials that gather various properties and functionalities in a single part. They are one of the few materials capable of recovering their original shape after a thermomechanical cycle and converting mechanical external stimuli into thermal response and vice-versa [1,2].

Due to these special properties, SMAs have been considered for several industrial applications. One of the most promising is the use of SMAs to drive small actuators. Such applications are based on the deformation of SMA components through martensitic transformation. The latter is a diffusionless process in which the crystal structure transforms from a parent (austenite) phase to a product phase (martensite), resulting in a considerable strain. This process can be triggered either by mechanical or thermal loading. Its activation can be controlled electrically via Joule heating. Thus, SMAs properties enable the design of compact and lightweight actuators [3].

Despite SMA actuators are very appropriate for several applications (e.g. small automotive and aeronautical devices), they are little exploited [4]. The major reasons for this are the complexity involving the modeling of their thermomechanical behavior and their functional properties degradation during use, also known as Functional Fatigue (FF).

The degradation in SMA properties is mainly originated from two sources: plasticity (dislocations) and residual martensite. The plasticity is commonly triggered through a slip in austenite phase at high temperatures [5–8] or during cycling where Transformation Induced Plasticity (TRIP) at austenite–martensite interfaces progressively accumulates. The latter is the most common in SMA actuators and is responsible for the decrease of the transformation start stress [9]. With regard to the residual martensite, the process involved in its apparition is in part linked to the dislocation accumulation [10–13] and partly to the applied external load [14,15]. Therefore, it is coupled with plasticity.

Macroscopic models considering the role of plasticity and/or residual martensite on the cyclic response of SMA have been proposed only for superelastic loading [9,14,16–19]. Fewer models were introduced considering the same problem under actuation conditions [15,20–22]. In addition, for the SMA actuator context, thermal exchange (convection and conduction) and its consequences on the behavior e.g. (thermomechanical coupling) also directly impact the actuation output. Other models were proposed to account for those effects [18,19,23–25], but none were extended to thermomechanical loading.

As Joule heating is the most common mean of activation of SMA actuators, the modeling of this phenomenon should also be included. Some works [26,27] addressed this topic separately from those previously mentioned.

A comparison between the main modeling strategies found in the literature can be established by using 3 criteria groups: loading nature,

* Corresponding author at: ENI Brest, UMR CNRS 6027, IRDL, F-29200, Brest, France.
E-mail address: lopes@enib.fr (M. Lopes Leal Júnior).

https://doi.org/10.1016/j.ijfatigue.2023.108055
Received 24 August 2023; Received in revised form 12 October 2023; Accepted 6 November 2023
Available online 8 November 2023

Table 1
Comparison between the main SMA Modeling strategies considering seven SMA features to be reproduced in a cyclic actuation context.

Reference	SMA features to reproduce						
	Uniaxial loading	TWSME	ASME	Thermomechanical coupling	Plastic accum.	FF	Joule heating
Bo and Lagoudas [14]	✓	✓	✓	×	✓	✓	×
Bouvet et al. [28]	✓	✓	✓	×	×	×	×
Auricchio et al. [29]	✓	✓	✓	×	✓	×	×
Morin et al. [30]	✓	✓	✓	✓	✓	×	×
Saint-Sulpice et al. [31]	✓	✓	✓	×	✓	✓	×
Chemisky et al. [21]	✓	✓	✓	×	✓	✓	×
Chemisky et al. [22]	✓	✓	✓	×	✓	✓	×
Talebi et al. [26]	✓	✓	×	×	×	×	✓
Shayanfard et al. [27]	✓	✓	×	✓	×	×	✓
Present work	✓	✓	✓	✓	✓	✓	✓

associated SMA-phenomena reproduction and cyclic usage context. The first group refers to the nature of the applied loading that the model is capable of reproducing (e.g. proportional/non proportional and multi-axial/uniaxial loads). The second one lists the main SMAs phenomena that can be represented in the material (e.g. Two-way Shape Memory Effect (TWSME), Assisted Shape Memory Effect (ASME), superelasticity, pseudoplasticity, reorientation, tension–compression asymmetric behavior, return point memory, R-phase effects, plastic yielding). At last, a division gathers the most common effects that can result from cyclic loading (e.g. thermomechanical coupling, plasticity accumulation and FF).

In order to reproduce the SMA actuator behavior during operation, the following features are strictly necessary in the modeling strategy (as it is detailed in Sections 2 and 3): uniaxial loading, TWSME, ASME, thermomechanical coupling, plasticity accumulation, evolution of the transformation strain and Joule heating. With this in mind, a comparison between the main modeling strategies and based on their capability to replicate these necessary features is given in Table 1.

As demonstrated in Table 1, although many modeling strategies were proposed in the past, none of them contemplates together the main phenomena involved in the real use of SMA actuators. Therefore, in order to fulfill this gap, a constitutive model and a straightforward numerical approach is here introduced to help designers and engineers to simulate the lifespan behavior of SMA actuators in an innovative way. The proposed model incorporates the main thermal exchange phenomena with the environment, the effects of electric activation via Joule heating, the FF evolution of the most important SMA features, and the thermomechanical coupling related to the actuation rate, faithfully reproducing the actuation scenario.

The work is organized as follows. A brief analysis of the main phenomena involved during the actuation of the most common SMA actuators is presented in Section 2. An analysis of the thermomechanical behavior of thin SMA wires under ASME loading via experimental testing is given in Section 3. The proposed modeling strategy, based on the experimental findings and on a reference model in literature is presented in Section 4 with the numerical implementation described in Section 5. To validate the introduced strategy, a comparison between experimental data and simulations is addressed in Section 6. The final remarks follow in conclusion section (Section 7).

2. Actuation through Joule effect

During the actuation of an SMA actuator, the phase transformation is triggered through heating and cooling process under mechanical loading. Therefore, several options of actuation are possible and it is up to the designers/engineers to find the best solution for the different actuation options. Another point to be considered is the evolution of the actuator's output (displacement of a rod, rotation of a pulley or other) during its lifespan: the FF. This last factor is mainly associated with the evolution of the SMA's microstructure during cycling and, it impacts directly on the macroscopic output parameters (transformation and residual strains).

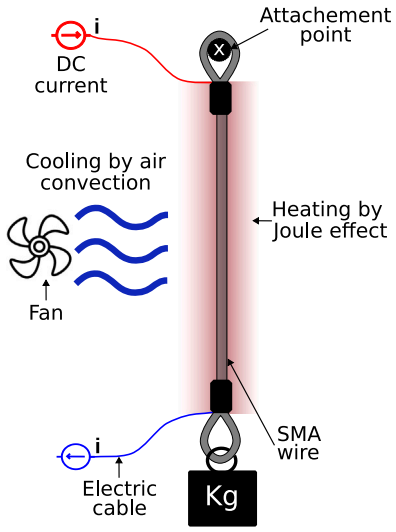

Fig. 1. Representation of the electrical–thermal–mechanical phenomena involved in SMA actuation. A SMA wire is heated through the flow of electric current (i), cooled by forced convection generated by fans and loaded by a dead weight, represented as 'Kg'.

For the heating of the SMA-actuator component, hereafter considered as a wire (the most implemented solution in literature [3,32].), two main options are employed: hot blowing air and electric current (*Joule effect*). The second solution is widely selected over the first due to its higher heating rate and easier implementation.

With respect to the cooling process, the heat exchange through convection is the most employed solution. For this, natural or forced convection as well as the exchange fluid (air, water or other liquid) can be selected depending on the project specifications. However, due to cost reduction and to the small size the majority of SMA actuator, the natural convection through air is the most employed method.

Depending on the desired displacement of the actuator (given by an output strain (ε^{output}) of the SMA component), a constant or variable load can be applied to the system. For this, dead weights, return springs or other pieces can be used to load and return the system to initial state.

In summary, all these factors will impact directly the response of the actuator during an actuation cycle. They are illustrated in Fig. 1. When a long-term use is considered, in addition to the aforementioned factors, the microstructural effects will also influence the actuator response and must be taken into account in the modeling strategy. These mechanisms are detailed in the following.

3. Experimental characterization of SMA actuators

During repeated actuation, SMA actuators exhibit a degradation in their performance. This degradation is called FF. Despite the great

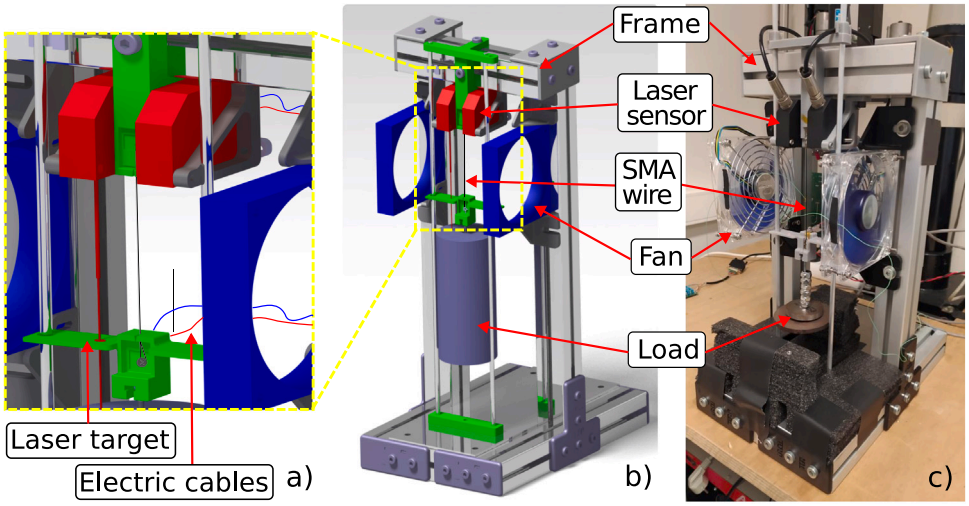

Fig. 2. *ad hoc* fatigue testing machine. (a) CAD detail. (b) CAD representation. (c) Photo of the built machine.

number of studies regarding the structural fatigue of SMAs, FF is less addressed. In addition, the majority of the works regarding FF in SMA focuses on the superelastic effect (isothermal loading). Given this context, the need for more extensive experimental data as well as analysis and tools to understand the mechanisms involved during thermal cycles is evident.

With this in mind, this section addresses the impact of the operational parameters (e.g. heating time, cooling time and applied stress) on the FF, through an experimental analysis. A method to identify the evolution of the functional properties is also presented and discussed in the following.

3.1. Experimental characterization procedure

0.19 mm diameter trained NiTi wires produced by Dynalloy® have been considered for the experimental tests to illustrate the actuation of an SMA actuator over its lifespan.

Thermomechanical loading experiments were performed using an *ad hoc* testing machine (Fig. 2). In such a machine, the SMA wires are heated through the Joule effect, cooled by two electric commanded fans and mechanically loaded via a dead weight. The actuator's mechanical response was measured by two laser sensors pointed to a target plate, positioned at the same height as the end of the SMA wire. This target plate composes the support part that is also responsible for electrically powering the wire and for attaching the dead weight. The imposed electric conditions (*HT*, *CT* and forced or natural convection regime) were commanded through an *ad hoc* program and recorded by sensors placed at a control board. To avoid any kind of noise during the measurements, the power supplies for the measurement devices and for the SMA wire were set distinctly.

Different testing conditions were applied by varying the constant mechanical load (σ), the maximum electric current (i), the heating time (HT) and the cooling time (CT) under a forced convection regime. Subsequently, the experimental data were processed and the functional parameters such as transformation strain (ε^{tr}) and residual strain (ε^{r}), were extracted for each cycle until failure or up to 130k cycles when the fatigue life was considered unlimited for this application and experiments were stopped.

The loading conditions were defined in a preliminary study in which, firstly, a differential scanning calorimetry test (DSC) was performed in order to evaluate the phase transformation temperatures of the employed wire. Then, a wide range of values for HT, CT and σ was tested, and only the sets of parameters that allow initial ε^{tr} bigger than 2.5% (herein considered minimum output strain level for this actuator) were chosen to be tested in a cyclic condition. Finally, the implemented loading conditions are defined in Table 2.

Table 2
Considered experimental testing conditions.

Test number	Stress, σ [MPa]	Heating time, HT [s]	Cooling time, CT [s]	Maximum current, i [A]
1	100	0.55	2	1
2	100	0.60	2	1
3	230	0.50	2	1
4	230	0.60	2	1
5	340	0.50	2	1
6	340	0.60	2	1

3.2. Experimental results

Given the experimental procedure, the evolution of the output strain (actuation strain) under different loading conditions is presented until 130k cycles. Fig. 3 shows the evolution of the output strain (related to the actuator displacement of the SMA component) for all tests. The evolution of the strain has a logarithmic form for all tests but different degradation rate is observed for each tested condition.

The latter is intimately associated with the microstructural evolution of SMA during cyclic loading, which makes challenging the analysis of the evolution of the output strain.

In order to link the measured strain to the underlying microstructural effects, a strain decomposition is proposed. This approach together with the analysis of other involved thermal phenomena is addressed in the following sections.

3.2.1. Microstructural mechanisms of the functional fatigue

The change in the macroscopic properties of the SMA actuators is directly associated with the microstructural evolution. Among the major actors to microstructure change during cyclic loading, the interactions between phase transformation and plasticity are the most significant.

The coupling between phase transformation and plasticity can occur in two different modes: upon repeated and far under yield strength loading and under thermomechanical conditions above the yield strength. For SMA actuators, the first mode is significantly more common.

Under cyclic loading, lattice defects accumulate due to the propagation of austenite/martensite interfaces. These defects are directly associated with plasticity (slip dislocations). As a result, residual stress-induced martensite (RSIM) is initiated due to internal stress accumulation [10,11,33] and the so-called Transformation Induced Plasticity (TRIP) is triggered as a main result of phase transformation coupling with plasticity [12,13,21,34]. Thus, RSIM and TRIP can be

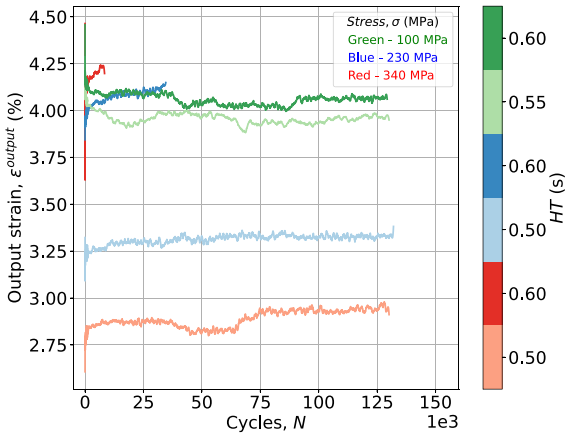

Fig. 3. Evolution of the output strain ϵ^{out} with the number of cycles. The implemented loading stresses σ are represented in three different colors. HT values are colored in different shades accordingly to the color of each level of σ.

directly associated with the FF. RSIM is easier to identify at supposedly pure austenite phase conditions and TRIP is present in both austenite and martensite phases. Hence, this work considers the microstructural changes by using two different strains related to the measured strain by $\epsilon^{output} = \epsilon^{tr} + \epsilon^{r}$. By using this decomposition, one can associate TRIP mechanisms with drift in both transformation strain ($\Delta\epsilon^{tr}$) and residual strains ($\Delta\epsilon^{r}$) and the RSIM mechanisms with residual strain drift only, as it is illustrated in Fig. 4.

To validate the source of the fatigue mechanisms affecting the FF, an experimental analysis was conducted using a resistivity measurement technique described in [8]. The resistivity analysis provides real-time information on the microstructural state of the SMA during loading through the measurement of a voltage variation. Therefore, this procedure is very useful for identifying the evolution of the microstructure when two different wire conditions (e.g. as received and cycled) are compared.

Two ASME tests were conducted on the same SMA wire at 230 MPa, both under quasi-static conditions. These tests were performed in tow separate occasions: one before subjecting the wire to 130k fatigue cycles on the *ad hoc* testing machine, and the other after. The testing condition for the fatigue test was identical to test number 3 in Table 2. Two graphics results as the output of these tests, one regarding the thermomechanical response and a second related to the electric behavior. The results are presented in Fig. 5.

First, regarding the thermomechanical response, one may note some of the well-known FF symptoms such as the reduction in the maximum transformation strain amount, the narrowing of the hysteresis and the evolution of the phase transformation temperatures. Second, by analyzing the electric response, a significant difference between the cycled and the as received condition can be noted, especially at higher temperatures. As represented by the dashed lines, the resistivity of pure states (e.g. stress-induced martensite or austenite) evolves linearly with temperature. Therefore, pure states can be easily identified in a resistivity analysis. Taking this into consideration, when comparing the resistivity values at approximately 145 °C, it is evident that in the cycled condition, the resistivity is significantly higher than in the as received condition. This increase in resistivity suggests the presence of martensite, which has a higher resistivity, even though it was expected to contain only the austenite phase. So, as aforementioned, the martensite present in this stage is known as RSIM, which results from a combination of internal stress accumulation. It is worth noting that plasticity induced by phase transformation is also present in the wire, meanwhile, the presence of dislocations in resistivity analysis is less perceptible.

In conclusion, the resistivity analysis presented evidence of the RSIM accumulation at high temperatures (by contrast to a supposedly pure austenite phase) and illustrated that the mechanisms involved in the FF are mainly due to the RSIM accumulation and the plasticity accumulation.

3.2.2. Strain degradation

Looking at the transformation strain degradation (Fig. 6), the higher value is found at the beginning of the lifespan. Then, an exponential evolution takes place until about 3–5k cycles. This stage is also called "accommodation", when the major changes in the microstructure take place. Finally, an almost linear evolution occurs and continues until the failure of the actuator.

Similar dynamics can be observed in the residual strain (Fig. 6). Although, in this case, the initial amount is zero and, then it rises exponentially during accommodation and then evolves linearly to its maximum value at the end of the lifespan. The described evolution is typical of this material and it agrees well with other studies [15,35,36].

Now, looking at the control parameters (σ and HT), one may note that they have a direct and strong impact on the evolution of the measured strain. With the increase of σ, the first stage of degradation seems to be more pronounced (3–5k cycles). This effect can be best observed in a logarithmic scale (Fig. 6), where a greater slope for bigger σ values is observed. Regarding the impact of the HT, it impacts directly the amount of initial transformation strain. For the tests with the same stress level, the higher the heating time, the higher is the initial transformation strain value (ϵ_0^{tr}). Therefore, it can be linked to the maximum amount of stress-induced martensite volume fraction transformed into austenite. A similar impact of HT on the residual strain evolution is observed.

4. Constitutive modeling

A literature review was performed in order to select the most adapted modeling strategy regarding the phenomena of interest in this study.

Several modeling strategies can be employed to simulate the behavior of SMAs. The models can be defined at macroscopic, micro and micro-macro scales. While macroscopic approaches mainly consider experimental and phenomenological observations to establish interactions between the involved mechanisms and their kinetics, the micro and micro-macro approaches use a wider phenomena data to process simulate pertinent characteristics at microscopic level. In micro approaches, the analysis is performed at the lattice level, typically using molecular dynamics theory and the description of effects such as nucleation or interface motion [37–40]. Regarding the context and the goals of this work, the macroscopic approaches (usage scale) was chosen. Therefore, the micro and micro-macro approaches will not be considered herein.

Table 1 shows that none of the cited modeling strategies fulfill the SMA features required in this work. However, some works [14,22,31] show closer compatibility with the requirements, with only the thermomechanical coupling and the Joule heating missing. Considering the available model extensions and also the compatibility with other less relevant SMA features, the modeling strategy initially proposed by Bo and Lagoudas [14] and later extended [21,22,41–44] was chosen as the base model to be extended for the approach developed in this study. In the next sections, the modifications to this modeling strategy are described as well as its numerical implementation.

4.1. Proposed model

Based on the modeling strategy proposed by Lagoudas et al. [43] and then extended for high-temperature SMA actuators by Chemisky et al. [22], a thermomechanical model for SMA actuator is here proposed. Here, modifications are considered to contemplate different phenomena such as FF, thermal exchange with the environment (heating by Joule effect and cooling by convection) and thermomechanical coupling effects due to phase transformation.

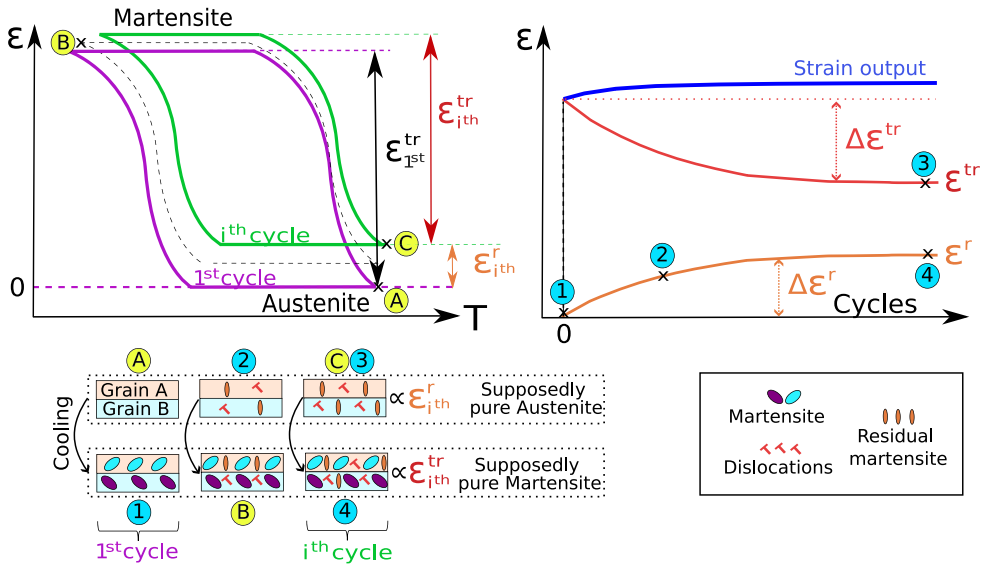

Fig. 4. Evolution of the FF and its corresponding mechanisms represented in the ε vs. T (upper left) and ε vs. Cycles (upper right) graphics and a bicrystal model (bottom part). The evolution of the FF regarding the ε vs. T is represented by the first and an arbitrary actuation cycles. The evolution of the FF with the number of cycles is represented in three different curves (ε^{out}, ε^{tr} and ε^{r}). The letters A to C refer to the supposedly pure states at different cycle numbers in the ε vs. T graphic, while the numbers 1 to 4 are related to the different evolution of ε^{tr} and ε^{r} with cycling.

4.1.1. Thermodynamical framework

Following the procedure applied on the aforementioned reference models, the Gibbs free energy potential can be written as a function of the applied stress tensor $\boldsymbol{\sigma}$ and absolute temperature T as external state variables and A^t as the set of internal state variables associated with the inelastic transformation process: G($\boldsymbol{\sigma}$, T, $\boldsymbol{A^t}$).

To be in accordance with the identified mechanism presented before, the set of internal state variables A^t is chosen as $\boldsymbol{A^t} = \left(\boldsymbol{\varepsilon^{tr}}, \boldsymbol{\varepsilon^{r}}, \xi, g^t\right)$, where: the transformation strain tensor $\boldsymbol{\varepsilon^{tr}}$ is the inelastic strain generated during phase transformation; the residual strain tensor $\boldsymbol{\varepsilon^{r}}$ is the inelastic strain associated to (RSIM) and also contains (TRIP) contributions ; the martensitic volume fraction ξ accounts for the generation and recovery of all martensitic variants and varies between $0 \leq \xi \leq 1$; and the transformation hardening energy g^t is a measure of the change in mixing energy. Thus, the Gibbs free energy is then decomposed in three components:

$$G\left(\boldsymbol{\sigma}, T, \boldsymbol{\varepsilon^{tr}}, \boldsymbol{\varepsilon^{r}}, \xi, g^t\right) = (1-\xi)G^A(\boldsymbol{\sigma}, T) + \xi G^M(\boldsymbol{\sigma}, T) + G^{\text{mix}}\left(\boldsymbol{\sigma}, \boldsymbol{\varepsilon^{tr}}, \boldsymbol{\varepsilon^{r}}, g^t\right),$$

where G^{γ} accounts for the thermoelastic free energy associated to pure states ($\gamma = A$ or M) and G^{mix} corresponds to a mixing energy term.

The total strain partition is given by:

$$\boldsymbol{\varepsilon} = \boldsymbol{\varepsilon^{el}} + \boldsymbol{\varepsilon^{th}} + \boldsymbol{\varepsilon^{tr}} + \boldsymbol{\varepsilon^{r}}. \tag{1}$$

By implementing the standard thermodynamical procedure defined by Coleman and Noll [45] and Coleman [46] the first law of thermodynamics can be expressed as:

$$\rho\dot{u} = \boldsymbol{\sigma} : \dot{\varepsilon} - div(\mathbf{q}) + \rho r, \tag{2}$$

where u is the mass-specific internal energy, $\mathbf{q}$ is the heat flux vector, and r is the rate of internal heat generation.

Similarly, the second law of thermodynamics (Clausius–Planck inequality) can be formulated as:

$$\rho\dot{s} + \frac{1}{T}div(\mathbf{q}) - \frac{\rho r}{T} \geqslant 0, \tag{3}$$

where s is the mass specific entropy. Multiplying Eq. (3) by T and substituting in Eq. (2) to eliminate div(q), we find:

$$\rho\dot{s}T + \boldsymbol{\sigma} : \dot{\varepsilon} - \rho\dot{u} \geqslant 0. \tag{4}$$

Considering the Gibbs free energy potential, given as:

$$G = u - \frac{1}{\rho}\boldsymbol{\sigma} : \boldsymbol{\varepsilon} - sT. \tag{5}$$

Substituting the time rate of change of Eq. (5) into Eq. (4), the Gibbs free energy rate is obtained:

$$-\rho\dot{G} - \dot{\boldsymbol{\sigma}} : \boldsymbol{\varepsilon} - \rho s\dot{T} \geqslant 0. \tag{6}$$

By applying the chain rule to G and using the set of internal variables defined in Eq. (1), we have:

$$-\rho(\partial_{\sigma}G : \dot{\boldsymbol{\sigma}} + \partial_T G\dot{T} + \partial_{\varepsilon^{tr}}G : \dot{\varepsilon}^{tr} + \partial_{\varepsilon^{r}}G : \dot{\varepsilon}^{r} + \partial_{\xi}G\dot{\xi} + \partial_{g^t}G\dot{g}^t) - \dot{\boldsymbol{\sigma}} : \boldsymbol{\varepsilon} - \rho s\dot{T} \geqslant 0,$$

where $\partial_j G$ is the partial derivative of G with respect to j. Then, by using the methodology of Coleman and Noll [45] and the terms from the latter equation, the state relations for the strain and entropy can be obtained:

$$\boldsymbol{\varepsilon} = -\rho\partial_{\sigma}G = \boldsymbol{S} : \boldsymbol{\sigma} + \boldsymbol{\alpha}\left(T - T_0\right) + \boldsymbol{\varepsilon^{tr}} + \boldsymbol{\varepsilon^{r}}, \tag{7}$$

$$s = -\partial_T G = \frac{1}{\rho}\boldsymbol{\alpha} : \boldsymbol{\sigma} + c\ln\left(\frac{T}{T_0}\right) + s_0. \tag{8}$$

From the remaining terms in Eq. (7), the generalized thermodynamical forces conjugated to the internal variables can be obtained. In this approach, the parameters ρ and $\boldsymbol{\alpha}$ denote the density and the thermal expansion tensor, respectively, and are assumed to be phase-independent. The other given parameters ($\boldsymbol{S}$, c, s_0 and T_0) are phase dependent and correspond to the elastic compliance tensor, specific heat, specific entropy at the reference state, specific internal energy at the reference state and the reference temperature, respectively. Additionally, considering a mixture law for the elastic compliance tensors (austenite and martensite), the current compliance tensor is obtained: $\boldsymbol{S} = \boldsymbol{S^{\mathcal{A}}} + \xi(\boldsymbol{S^{\mathcal{M}}} - \boldsymbol{S^{\mathcal{A}}})$.

$$-\rho\partial_{\xi}G = p, \quad -\rho\partial_{\varepsilon^{tr}}G = \boldsymbol{\sigma}, \quad -\rho\partial_{\varepsilon^{r}}G = \boldsymbol{\sigma}, \quad -\rho\partial_{g^t}G = -1. \tag{9}$$

By using the obtained relations, the second law can be rewritten as:

$$p\dot{\xi} + \boldsymbol{\sigma} : (\dot{\varepsilon}^{tr} + \dot{\varepsilon}^{r}) - \dot{g}^t \geqslant 0, \tag{10}$$

where p is the generalized thermodynamic force and can be expressed as:

$$p = \frac{1}{2}\boldsymbol{\sigma} : \Delta\boldsymbol{S} : \boldsymbol{\sigma} + \boldsymbol{\sigma} : \Delta\boldsymbol{\alpha}\left(T - T_0\right) - \rho\Delta c\left[\left(T - T_0\right) - T\ln\left(\frac{T}{T_0}\right)\right] + \rho\Delta s_0 T - \rho\Delta u_0, \tag{11}$$

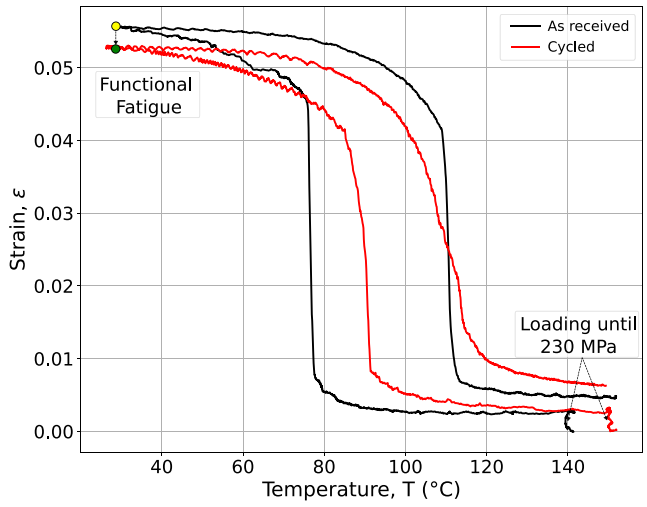

(a) Thermomechanical response.

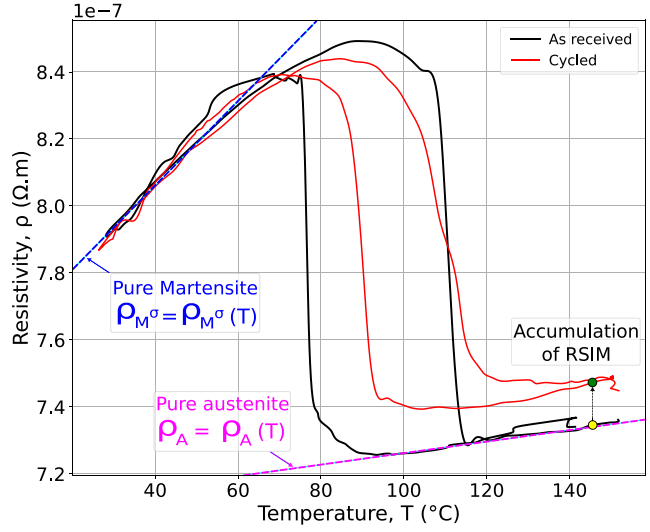

(b) Electric response

Fig. 5. Comparison between an as received and a cycled wire. In graphic a), strain degradation is represented by the yellow and green dots and the elastic loading until 230 MPa before the temperature variation is indicated by arrows. In graphic b), the dashed lines represent the evolution of the resistivity with temperature for pure states. The yellow and green dots represent the RSIM accumulation after cycling.

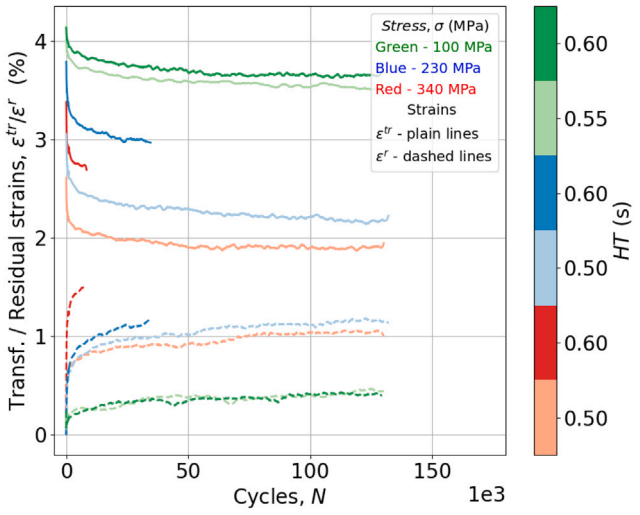

(a) Normal scale.

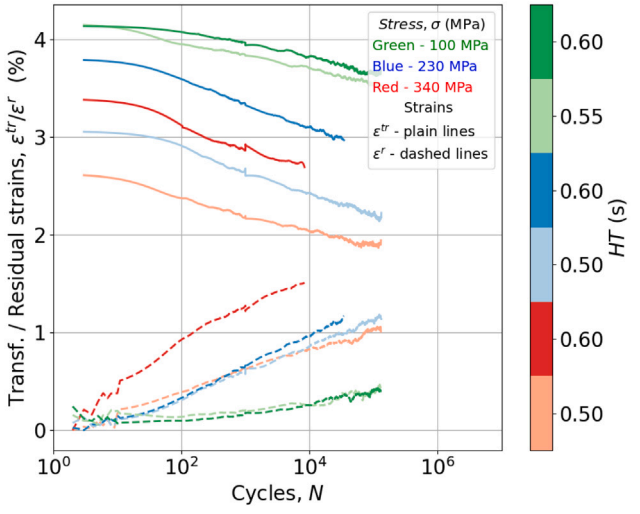

(b) Logarithmic scale.

Fig. 6. Transformation and Residual strain evolution in normal and logarithmic scales. The implemented σ are represented in three different colors. HT values are colored in different shades accordingly to the color of each level of σ.

where the operator Δ denotes the difference of material constant between pure states (A and M). As for s_0, u_0 is phase dependent and correspond to specific internal energy at the reference state.

As all internal variables are associated to the evolution of ξ, one may define all the thermodynamic forces conjugate to ξ as:

$$\left(\boldsymbol{\sigma} : \left(\Lambda^t + \Lambda^r\right) + p - f^t\right)\dot{\xi} = \pi^t\dot{\xi} \geqslant 0, \tag{12}$$

where π^t includes the coupled contributions of transformation and residual strain, the hardening energy evolution f^t (described in the following) as well as the transformation dissipation.

Finally, the decomposed Gibbs free energy terms (G^γ and G^{mix}) can be rewritten as:

$$G^\gamma(\boldsymbol{\sigma}, T) = -\frac{1}{2\rho}\boldsymbol{\sigma} : \boldsymbol{S}^\gamma : \boldsymbol{\sigma} - \frac{1}{\rho}\boldsymbol{\sigma} : \boldsymbol{\alpha}\left(T - T_0\right) + c^\gamma\left[\left(T - T_0\right) - T\ln\left(\frac{T}{T_0}\right)\right] - s_0^\gamma T + u_0^\gamma, \tag{13}$$

$$G^{mix}\left(\boldsymbol{\sigma}, \boldsymbol{\varepsilon}^{tr}, \boldsymbol{\varepsilon}^{r}, g^t\right) = -\frac{1}{\rho}\boldsymbol{\sigma} : \left(\boldsymbol{\varepsilon}^{tr} + \boldsymbol{\varepsilon}^{r}\right) + \frac{1}{\rho}g^t. \tag{14}$$

4.1.2. Conservation of energy

In this section, the thermomechanical coupling and the intrinsic dissipation terms are considered for SMA actuator under uniaxial loading in order to establish the equilibrium equation of heat for the present model.

By manipulating the two principles of thermodynamics, the following form of the conservation of energy is obtained:

$$-\rho T\frac{\partial^2 G}{\partial\boldsymbol{\sigma}\partial T} : \dot{\boldsymbol{\sigma}} - \rho T\frac{\partial^2 G}{\partial T^2}\dot{T} - \rho T\frac{\partial^2 G}{\partial \boldsymbol{A}_i\partial T} : \dot{\boldsymbol{A}}_i - D_i = -div(\mathbf{q}) + \rho r, \tag{15}$$

By considering the intrinsic dissipation (Eq. (12)), the equation can be reduced to

$$T\boldsymbol{\alpha} : \dot{\boldsymbol{\sigma}} - \rho c\Delta T + \left(-\pi^t + \rho\Delta s_0 T\right)\Delta\xi = -div(\boldsymbol{q}) + \rho r, \tag{16}$$

where c is the specific heat capacity (assumed equal for both austenite and martensite phases), π^t is the effective thermodynamic driving force

for transformation, $q \in \Re^3$ is the heat flux vector, and r is the specific heat source/sink term.

For the studied form of the actuator (thin wire), the heat transfer due to conduction through the cross-section and through the axial direction is assumed very small compared to convection heat transfers, therefore conduction effects are neglected. Then, the heat transfer through convection for a circular cross-section under one-dimensional assumptions can be written, leading to the heat flux vector:

$$q(T) = -\frac{A_{wire}}{V_{wire}} h(T - T_{amb}) = -\frac{4h}{d}(T - T_{amb}), \tag{17}$$

where h is the heat convection coefficient, d is the diameter of the considered wire, A_{wire} and V_{wire} are the surface and the volume of the wire, respectively, and T_{amb} is the room temperature.

Substituting Eq. (17) into Eq. (16) and considering the one-dimensional assumptions, the following simplified conservation of energy equation proposed by Tabesh et al. [44] is obtained:

$$T\alpha\dot{\sigma} - \rho c \Delta T + \left(-\pi^t + \rho \Delta s_0 T\right) \Delta\xi = q(T) + \rho r, \tag{18}$$

4.1.3. Evolution equations

Here, the main identified evolution mechanisms in SMA actuator are expressed through the strain tensors and the hardening energy.

First, to describe the evolution of the transformation and residual strain tensors during thermomechanical cycles, the accumulated detwinned martensite volume fraction (ζ^d) is employed as drive variable. This parameter was first introduced by Bo and Lagoudas [14] and it is expressed as:

$$\zeta^d = \int \dot{\xi}^d(\tau) d\tau, \tag{19}$$

where, $\dot{\xi}^d$ represents the rate of detwinned martensite volume fraction formed during a cycle and it is proportional to the rate of martensite volume fraction with proportionality constant $\frac{H^{\text{cur}}}{H_{\text{sat}}}$.

$$\dot{\xi}^d = \frac{H^{\text{cur}}}{H_{\text{sat}}} \dot{\xi}, \tag{20}$$

H^{cur} is the uniaxial maximum transformation strain magnitude for full transformation and it depends on the effective stress ($H^{cur} = H^{cur}(\bar{\sigma})$), which is defined in the Mises sense as:

$$\bar{\sigma} = \sqrt{\frac{3}{2}\boldsymbol{\sigma}' : \boldsymbol{\sigma}'}, \tag{21}$$

where σ' is the deviatoric part of the stress tensor.

To account for the dependency of H^{cur} on the stress level, Hartl et al. [47] proposed an exponential function based on empirical evidences. The values of H^{cur} vary between a minimum quantity when not mechanically loaded (H_{min}), corresponding to the Two Way Shape Memory effect (TWSME) and a saturation value (H_{sat}) when loaded. The transition between two maximum strain levels is governed by two parameters: the critical stress magnitude ($\bar{\sigma}_{crit}$), which denotes the initial transition point from H_{min} to H_{sat} and k that controls the rate of exponential evolution between these same two levels. Finally, the function is given by the following equation:

$$H^{cur}(\bar{\sigma}) = \begin{cases} H_{min}; & \bar{\sigma} \leqslant \bar{\sigma}_{crit}, \\ H_{min} + \left(H_{sat} - H_{min}\right)\left(1 - e^{-k\left(\bar{\sigma} - \bar{\sigma}_{crit}\right)}\right); & \bar{\sigma} > \bar{\sigma}_{crit}. \end{cases} \tag{22}$$

Once the description of the cyclic driven parameters is given, the strain tensors can be defined. As shown by the experiments, unrecoverable inelastic strain is accumulated during actuation mainly due to TRIP and RSIM mechanisms. However, dissociating these mechanisms is difficult. Therefore, the accumulation of unrecoverable strain is inserted in both transformation and residual strains to be directly compared to the macroscopic experimental observations.

In this work, we consider the transformation unrecoverable part to be related to TRIP accumulation effects and the residual unrecoverable strain to be associated to RSIM and to TRIP. Consequently, both strains are dependent on the history of the martensitic phase transformation [14,21]. Thus, the transformation strain definition of [14,21,22] is modified by considering the logarithmic-type trends observed in the experimental analysis instead of exponential-type curves. So, the transformation tensor during forward ($\dot{\xi} > 0$) and reverse transformation ($\dot{\xi} < 0$) is defined as:

$$\dot{\varepsilon}^{tr} = \Lambda^t \dot{\xi}, \quad \Lambda^t = \begin{cases} \Lambda^t_{fwd}, & \dot{\xi} > 0 \\ \Lambda^t_{rev}, & \dot{\xi} < 0 \end{cases} \tag{23}$$

$$\Lambda^t_{fwd} = \frac{3}{2} H^{cur} \frac{\boldsymbol{\sigma}'}{\bar{\sigma}} \left(a_{tr} log(\zeta^d) + 1\right), \tag{24}$$

$$\Lambda^t_{rev} = \frac{\boldsymbol{\varepsilon}^{t-r}}{\xi^{t-r}} \left(a_{tr} log(\zeta^d) + 1\right), \tag{25}$$

In Eqs. (24) and (25) the term in parenthesis account for the cyclic evolution, commanded by the material parameters a_{tr} and b_{tr}. Additionally, $\boldsymbol{\varepsilon}^{t-r}$ and ξ^{t-r} correspond to the macroscopic transformation strain and to martensite volume fraction at the reversal transformation, respectively.

Considering the same approach as for transformation strain and inspired by the work of Lagoudas and Entchev [16] and Chemisky et al. [21], the residual direction tensor is defined as:

$$\dot{\varepsilon}^r = \Lambda^r \dot{\xi}, \quad \Lambda^r = \begin{cases} \Lambda^r_{fwd}, & \dot{\xi} > 0 \\ \Lambda^r_{\text{rev}}, & \dot{\xi} < 0 \end{cases} \tag{26}$$

Λ^r_{fwd} is the residual direction tensor during the forward transformation and Λ^r_{rev} during the reverse transformation. Although there is no general agreement if the triggering of residual strain mostly takes place during the forward, reverse or in both transformations, some authors [5,48] showed that the applied stress levels are one key to this process. Under low stress levels (as the ones evaluated in this work) the plastic mechanisms are hardly activated during reverse transformation. Hence, in this work, the residual strain is considered to take place only during the forward transformation. Finally, the two tensors are defined as:

$$\Lambda^r_{fwd} = \frac{3}{2} \frac{\boldsymbol{\sigma}'}{\bar{\sigma}} \left(a_r log(-\zeta^d)\right), \tag{27}$$

$$\Lambda^r_{rev} = 0. \tag{28}$$

Finally, an evolution equation is also needed to link the time rate of change of the hardening energy ($\dot{g}^t$) to that of the volume fraction of martensite $\dot{\xi}$:

$$\dot{g}^t = f^t \dot{\xi}, \quad f^t = \begin{cases} f^t_{fwd}, & \dot{\xi} > 0, \\ f^t_{rev}, & \dot{\xi} < 0, \end{cases} \tag{29}$$

where f^t is the hardening function that describes smooth transition from elastic to transformation response [43]. The hardening functions are given by:

$$\begin{aligned} f^t_{\text{fwd}}(\xi) &= \frac{1}{2} a_1 \left(1 + \xi^{n_1} - (1 - \xi)^{n_2}\right) + a_3, \\ f^t_{\text{rev}}(\xi) &= \frac{1}{2} a_2 \left(1 + \xi^{n_3} - (1 - \xi)^{n_4}\right) - a_3. \end{aligned} \tag{30}$$

The exponents n_1, n_2, n_3 and n_4 are real values in the interval (0, 1) and are determined from calibration to best fit the martensite transformation hysteresis. The remaining coefficients (a_1, a_2, a_3 and a_4) are model parameters that characterize the martensite transformation.

4.1.4. Transformation critical thermodynamic forces

With the evolution equations and the thermodynamic conditions determined, two critical thermodynamic driving forces functions are

necessary to establish the start and to maintain the martensite transformation [41]. These functions are denoted as Y^t_{fwd} and Y^t_{rev} and intervene in the transformation functions Φ^t_{fwd} and Φ^t_{rev}.

The following forms of Y^t_{fwd} and Y^t_{rev} are assumed [47]:

$$Y^t_{fwd}(\boldsymbol{\sigma}) = Y^t_0 + D\boldsymbol{\sigma} : \left(\boldsymbol{\Lambda^t} + \boldsymbol{\Lambda^r}\right), \tag{31}$$

$$Y^t_{rev}(\sigma) = Y^t_0 + D\boldsymbol{\sigma} : \left(\boldsymbol{\Lambda^t} + \boldsymbol{\Lambda^r}\right), \tag{32}$$

where D is a model parameter that allows to represent the stress dependency of the critical thermodynamical forces and Y^t_0 is a constant parameter.

The forward phase transformation function is given by:

$$\Phi^{\mathrm{t}}_{fwd}(\boldsymbol{\sigma}, T, \xi) = \pi^{\mathrm{t}}_{fwd} - Y^{\mathrm{t}}_{fwd}, \tag{33}$$

and based on the Kuhn–Tucker conditions it implies that:

$$\dot{\xi} \geqslant 0, \quad \Phi^t_{fwd} \leqslant 0, \quad \Phi^t_{fwd}\dot{\xi} = 0. \tag{34}$$

Following the same procedure, the reverse transformation function is given by:

$$\Phi^{\mathrm{t}}_{rev}(\boldsymbol{\sigma}, T, \xi) = -\pi^{\mathrm{t}}_{rev} + Y^{\mathrm{t}}_{rev}, \tag{35}$$

and based on the Kuhn–Tucker conditions it implies that:

$$\dot{\xi} \leqslant 0, \quad \Phi^t_{rev} \leqslant 0, \quad \Phi^t_{rev}\dot{\xi} = 0. \tag{36}$$

4.1.5. One-dimensional reduction

The described relations in the previous sections can be expressed in the form of 20 scalar equations: (a) the evolution of transformation strain (Eq. (23)), (b) the evolution of residual strain (Eq. (26)), (c) the evolution of hardening energy (Eq. (29)), (d) the strain decomposition (Eq. (7)), (e) the Kuhn–Tucker condition for transformation (Eq. (34) or Eq. (36)). Together with the 20 scalar unknowns $\left(\boldsymbol{\sigma}, \boldsymbol{\varepsilon^{tr}}, \boldsymbol{\varepsilon^r}, \xi, \text{ and } g^t\right)$, it is possible to solve the system given a stress and temperature increment.

As the mechanical loading for the considered SMA-based actuator is an uniaxial loading (tension along a wire), the model parameters can be reduced to a one-dimensional case, where $\boldsymbol{\sigma}$ can be reduced to σ_{11} ($\sigma_{ij} = 0$). The transformation and residual strain components are given as :

$$\varepsilon^{tr}_{11} = \varepsilon^{tr}, \quad \varepsilon^{tr}_{22} = \varepsilon^{tr}_{33} = -\frac{1}{2}\varepsilon^{tr} \quad \varepsilon^{tr}_{ij} = 0, \tag{37}$$

and,

$$\varepsilon^{r}_{11} = \varepsilon^{r}, \quad \varepsilon^{r}_{22} = \varepsilon^{r}_{33} = -\frac{1}{2}\varepsilon^{r} \quad \varepsilon^{r}_{ij} = 0. \tag{38}$$

Thus, the strain decomposition is given as:

$$\varepsilon = \varepsilon^{el} + \varepsilon^{th} + \varepsilon^{tr} + \varepsilon^{r}, \tag{39}$$

Then, the relation between stress and strain reduces to:

$$\sigma = E(\xi)\left[\varepsilon - \alpha\left(T - T_0\right) - \varepsilon^{tr} - \varepsilon^{r}\right] \tag{40}$$

where E is defined as:

$$E(\xi) = \left[1/E^A + \xi\left(1/E^M - 1/E^A\right)\right]^{-1} \tag{41}$$

The evolution equations for the transformation and the residual strain reduce into:

$$\dot{\varepsilon^{tr}} = \Lambda^t\dot{\xi}; \quad \Lambda^t = \begin{cases} H^{cur}(\sigma)(a_{tr}log(\zeta^d) + 1)\,\mathrm{sgn}(\sigma), & \xi > 0, \\ (a_{tr}log(\zeta^d) + 1)\varepsilon^{t-r}/\xi^{t-r}; & \xi < 0. \end{cases} \tag{42}$$

$$\dot{\varepsilon^{r}} = \Lambda^r\dot{\xi}; \quad \Lambda^r = \begin{cases} a_r log(\zeta^d), & \xi > 0, \\ 0, & \xi < 0. \end{cases} \tag{43}$$

By considering Δc and $\Delta\alpha$ nulls (common engineering assumptions) and that the evolution of the hardening energy remains unchanged from Eq. (29), the transformation function during forward transformation simplifies to:

$$\Phi^t_{\mathrm{fwd}}(\sigma, T, \xi) = (1 - D)\left(\Lambda^t_{fwd} + \Lambda^r_{fwd}\right)\sigma + \frac{1}{2}\left(\frac{1}{E^M} - \frac{1}{E^A}\right)\sigma^2 + \rho\Delta s_0 T - \rho\Delta u_0 - f^t_{\mathrm{fwd}}(\xi) - Y^t_0 = 0, \tag{44}$$

and for reverse transformation it is given by:

$$\Phi^t_{rev}(\sigma, T, \xi) = -(1 + D)\left(\Lambda^t_{rev} + \Lambda^r_{rev}\right)\sigma - \frac{1}{2}\left(\frac{1}{E^M} - \frac{1}{E^A}\right)\sigma^2 - \rho\Delta s_0 T + \rho\Delta u_0 + f^t_{rev}(\xi) - Y^t_0 = 0. \tag{45}$$

5. Numerical implementation of the constitutive model

Once the description of the proposed constitutive model is given and the most important actuation factors are incorporated into the heat equation, the numerical implementation procedure can be described.

As the model accounts for thermomechanical and thermoelectrical couplings, a resolution strategy for this problem is proposed based on [49,50] work: a weak coupling method used to resolve the partial differential equations sequentially.

Firstly, an electrical analysis is performed considering the electrical input on the system (i_{n+1}) and the heat exchange with the surroundings via convection. Secondly, a thermo-elastic prediction accounting for the heat generated in the previous stage is evaluated. Then, if the predicted thermoelastic state violates the transformation criterion ($\Phi^t_{fwd} > 0$ or $\Phi^t_{rev} > 0$), the evolution of ε^{tr} and ε^r can be incrementally evaluated by using an implicit integration scheme that accounts for the thermomechanical coupling. For this stage, a return mapping algorithm (RMA) [51] is used to evaluate the model increment outputs for a given stress and temperature increments. Finally, this procedure is repeated over again until the convergence criteria are satisfied. Fig. 7 presents a flowchart of the described strategy.

In the sequel, subscript (n) refers to the time step and the indices (k) and $(k + 1)$ denote the number of iterations in the SMA thermomechanical analysis stage and during a time step (n).

5.1. Electrical analysis

As aforementioned the main heating principle implemented for SMA-based actuators is the Joule effect. Therefore, for the first stage of the numerical implementation, the total electrical energy provided to the actuator is considered to be completely converted into heat. Thus, the added energy in the system is considered as the heat source/sink term in Eq. (18). To evaluate this term, the density of heat (q_c) developed by DC current (i) passing through a homogeneous conductor is expressed as [52]:

$$q_c = \frac{i^2 R}{V_{wire}}, \tag{46}$$

The electrical resistance can also be expressed as:

$$R = \frac{\rho^{electric} L}{A_{wire}}, \tag{47}$$

where, $\rho^{electric}$ is the electrical resistivity of the wire, here considered as temperature and martensite volume fraction dependent ($\rho^{electric} = \rho^{electric}(\xi, T)$). L is the total length of the wire actuator. Substituting Eq. (47) in Eq. (46) we obtain the density of heat as a function of electrical resistivity.

$$q_c = \frac{\rho^{electric} L}{A_{wire}}\frac{i^2}{V_{wire}} \Rightarrow q_c = \rho^{electric}\left(\frac{4i}{\pi d^2}\right)^2. \tag{48}$$

Considering a time period (Δt), the previous equation can be expressed as the heat source/sink term.

$$\rho r = \rho.\rho^{electric}\left(\frac{4i}{\pi d^2}\right)^2 \Delta t. \tag{49}$$

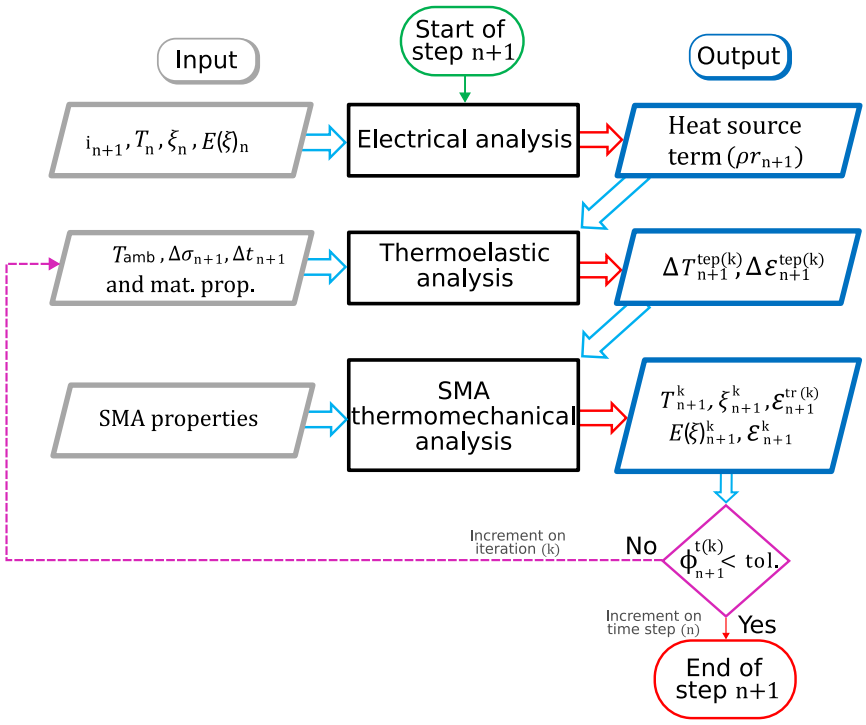

Fig. 7. Numerical integration method flowchart.

At this stage, the electrical resistivity value is estimated by using the temperature and martensitic volume fraction from the previous time step (n). This approximation is applicable since the resistivity value varies very little with small stress and current increments.

The heat source/sink term is then evaluated and will be the input of the next stage.

5.2. Thermoelastic prediction analysis

In the second stage, the prediction of the stress and temperature terms is considered, $\Delta\boldsymbol{\varepsilon}^{tep(k)}_{n+1}$ and $\Delta T^{tep(k)}_{n+1}$, respectively. At this step, no phase transformation is supposed to occur and, therefore, no transformation or residual strain is produced ($\Delta\xi = \Delta\boldsymbol{\varepsilon}^{tr} = \Delta\boldsymbol{\varepsilon}^{r} = 0$) and the variables values that are dependent on the martensite volume fraction ($\boldsymbol{S}$) are consider the same as in the previous step (n). To evaluate the increments in stress and temperature, the incremental forms of Eqs. (7), (16) and (17) are considered. These forms are given by:

$$T_n\boldsymbol{\alpha} : \Delta\boldsymbol{\sigma}_{n+1} - \rho c\Delta T^{tep(k)}_{n+1} = (q(T_n) + \rho r)\Delta t, \tag{50}$$

$$\Delta\boldsymbol{\varepsilon}_{n+1} = \boldsymbol{S}_n\Delta\boldsymbol{\sigma}_{n+1} - \boldsymbol{\alpha}\Delta T^{tep(k)}_{n+1} \tag{51}$$

Then, by solving the linear system formed by Eqs. (50) and (51), we find the thermoelastic prediction increments $\Delta T^{tep(k)}_{n+1}$ and $\Delta\boldsymbol{\varepsilon}^{tep(k)}_{n+1}$:

$$\Delta T^{tep(k)}_{n+1} = -\frac{\left(q(T_n) + \rho r\right)\Delta t}{\rho c} + \frac{T_n}{\rho c}\left(\Delta\boldsymbol{\alpha} : \boldsymbol{\sigma}_{n+1}\right), \tag{52}$$

$$\Delta\boldsymbol{\varepsilon}^{tep(k)}_{n+1} = \boldsymbol{S}_n\Delta\boldsymbol{\sigma}_{n+1} - \frac{\left(q(T_n) + \rho r\right)\Delta t}{\rho c}\boldsymbol{\alpha} + \frac{T_n}{\rho c}\boldsymbol{\alpha}\left(\boldsymbol{\alpha} : \Delta\boldsymbol{\sigma}_{n+1}\right). \tag{53}$$

The aforementioned increments are then used to evaluate temperature and strain corresponding to both stress and heat source/sink term input increments during the considered time step.

5.3. SMA thermomechanical analysis

For the last stage, the goal is to solve the thermoelastic-transformation problem defined by the total strain relation Eq. (7), the flow rules Eqs. (34) and (36), and the transformation function Eqs. (33) and (35).

After the thermoelastic prediction, if the phase transformation is to take place ($\Phi^{t}_{fwd} \geq 0$ or $\Phi^{t}_{rev} \geq 0$), several iterative corrections are performed until the re-establishment of the consistency condition. Following the established procedure in [41], the closest point projection scheme gives the iterative-incremental relation for Eqs. (23) and (26):

$$\boldsymbol{\varepsilon}^{tr(k+1)}_{n+1} = \boldsymbol{\varepsilon}^{tr(k)}_{n+1} + \Delta\boldsymbol{\varepsilon}^{tr(k)}_{n+1}, \tag{54}$$

where $\Delta\boldsymbol{\varepsilon}^{tr(k)}_{n+1}$ after some simplifications is given as:

$$\Delta\boldsymbol{\varepsilon}^{tr(k)}_{n+1} = \Delta\xi^{(k)}_{n+1}\boldsymbol{\Lambda}^{t}\left(\boldsymbol{\sigma}^{(k)}_{n+1}\right). \tag{55}$$

Likewise, the iterative update for the other strain is given by:

$$\Delta\boldsymbol{\varepsilon}^{th(k)}_{n+1} = \boldsymbol{\alpha}\Delta T^{(k)}_{n+1}, \quad \Delta\boldsymbol{\varepsilon}^{el(k)}_{n+1} = \frac{\boldsymbol{\sigma}^{(k)}_{n}}{E^{(k)}_{n}(\xi)} + \Delta\boldsymbol{S} : \boldsymbol{\sigma}^{(k)}_{n+1}, \quad \Delta\boldsymbol{\varepsilon}^{r(k)}_{n+1} = \Delta\xi^{(k)}_{n+1}\boldsymbol{\Lambda}^{r}\left(\boldsymbol{\sigma}^{(k)}_{n+1}\right). \tag{56}$$

The decomposition of incremental strains is given by:

$$\Delta\boldsymbol{\varepsilon}^{(k)}_{n+1} = \Delta\boldsymbol{\varepsilon}^{el(k)}_{n+1} + \Delta\boldsymbol{\varepsilon}^{th(k)}_{n+1} + \Delta\boldsymbol{\varepsilon}^{tr(k)}_{n+1} + \Delta\boldsymbol{\varepsilon}^{r(k)}_{n+1}. \tag{57}$$

Given Eq. (56) and considering that the stress increment is null ($\Delta\boldsymbol{\sigma}^{(k)}_{n+1} = 0$), Eq. (57) can be rewritten as:

$$\Delta\boldsymbol{\varepsilon}^{(k)}_{n+1} = \Delta\boldsymbol{S} : \boldsymbol{\sigma}^{(k)}_{n+1}\Delta\xi^{(k)}_{n+1} + \boldsymbol{\alpha}\Delta T^{(k)}_{n+1} + \boldsymbol{\Lambda}^{t}\left(\boldsymbol{\sigma}^{(k)}_{n+1}\right)\Delta\xi^{(k)}_{n+1} + \boldsymbol{\Lambda}^{r}\left(\boldsymbol{\sigma}^{(k)}_{n+1}\right)\Delta\xi^{(k)}_{n+1}. \tag{58}$$

In order to verify the consistency condition in the next iterations, the following is necessary:

$$\phi^{t(K)}_{n+1} + \Delta\phi^{t(K)}_{n+1} = \phi^{t(k+1)}_{n+1} \simeq 0. \tag{59}$$

Applying the chain rule to the last:

$$\phi^{(k)}_{n+1} + \partial_\sigma\Phi^{(k)}_{n+1} : \Delta\boldsymbol{\sigma}^{(k)}_{n+1} + \partial_T\phi^{(k)}_{n+1}\Delta T^{(k)}_{n+1} + \partial_\xi\phi^{(k)}_{n+1}\Delta\xi^{(k)}_{n+1} \simeq 0 \tag{60}$$

The obtained relation can be simplified by considering again that the stress increment is null $\left(\Delta\boldsymbol{\sigma}^{(k)}_{n+1}\right)$:

$$\phi^{(k)}_{n+1} + \partial_T\phi^{(k)}_{n+1}\Delta T^{(k)}_{n+1} + \partial_\xi\phi^{(k)}_{n+1}\Delta\xi^{(k)}_{n+1} \simeq 0, \tag{61}$$

Table 3
Necessary material parameters for the model.

Model parameter	Symbols (unit)	Identified	Values from literature
Thermoelasticity			
Young's modulus	E^A, E^M (GPa)	73, 37	46, 25 Lagoudas and Entchev [16]
Thermal expansion coefficients	α^A, α^M (K^{-1})	–	11E−6, 6E−6 Lagoudas and Entchev [16]
Phase transformation			
Transformation slopes	C^A, C^M (MPa K^{-1})	6.9, 9.9	8.3, 6.7 [22]
Hardening parameters	n_1, n_2, n_3, n_4	–	0.17, 0.27, 0.25, 0.35 [32]
Cycling			
Evolution coef. for transf. strain	a_{tr}	−3.3E−5	–
Evolution coef. for residual strain	a_r	8.6E−6	–
Thermal exchange			
Convection coefficient	h (W/m^2 K)	350	100 [44]
Density	ρ (kg/m^3)	–	6500 [44]
Specific heat	c (J/kg K)	–	400 [44]
Electrical parameters			
Slope of pure A and M	μ_A, μ_M	0.34E−9, 1.34E−9	–
Initial resistivity of pure A and M	ρ_A, ρ_M	7.07E−7, 7.69E−7	–

Now, the thermomechanical coupling due to the phase transformation is introduced in the problem via the incremental version of the heat equation (Eq. (18)), rewritten considering $\left(\Delta\boldsymbol{\sigma}_{n+1}^{(k)}\right)$:

$$-\rho c\Delta T_{n+1}^{(k)} + \left(-\pi_{n+1}^{t(k)} + \rho\Delta s_0 T_{n+1}^{(k)}\right)\Delta\xi_{n+1}^{(k)} = q(T) + \rho r, \tag{62}$$

Since the heat source/sink term was already considered in this step at the first stage and assuming no heat exchange with surroundings during the phase transformation, a simplified relation is obtained:

$$-\rho c\Delta T_{n+1}^{(k)} + \left(-\pi_{n+1}^{t(k)} + \rho\Delta s_0 T_{n+1}^{(k)}\right)\Delta\xi_{n+1}^{(k)} = 0, \tag{63}$$

Finally, for each correction iteration, the following linear system of two equations (Eq. (61) and Eq. (63)) with two unknowns $\Delta\xi_{n+1}^{(k)}$ and $\Delta T_{n+1}^{(k)}$ is solved:

$$\begin{bmatrix} \partial_{\xi}\boldsymbol{\Phi}_{n+1}^{t(k)} & \partial_{T}\boldsymbol{\Phi}_{n+1}^{t(k)} \\ -\pi_{n+1}^{t(k)} + \rho\Delta s_0 T_{n+1}^{(k)} & \rho c \end{bmatrix} \begin{bmatrix} \Delta\xi_{n+1}^{(k)} \\ \Delta T_{n+1}^{(k)} \end{bmatrix} = \begin{bmatrix} -\boldsymbol{\Phi}_{n+1}^{t(k)} \\ 0 \end{bmatrix} \tag{64}$$

Once the $\xi_{n+1}^{(k)}$ and $\Delta T_{n+1}^{(k)}$ increments are evaluated, the other variables are updated. Then, the consistency condition is compared with a tolerance value. If the value is within the limits, the step is concluded, otherwise, a new iteration will start.

6. Simulation results and validation

In this section, the modeling results of the proposed model are compared with the acquired experimental data for a given test under the following conditions: ∅0,19 mm (wire diameter), σ = 100 MPa, HT = 0.7 s, CT = 3 s and i = 1 A. The room temperature was considered as 20 °C.

In addition to the acquired experimental data for fatigue tests, temperature measurement was performed by using an infrared thermal camera (Infratec). The following temperature measurements correspond to the maximum evaluated value along the wire. Regarding the numerical model, the employed material parameters are listed in Table 3. Some of the parameters were identified by experimental characterization. The experimental tests and more details are presented in Appendix. For the unidentified parameters, the values from literature were used. The used input parameters (listed in Table 4).

Three main actuation parameters are here compared: total strain, temperature and current.

Table 4
Input model parameters.

Input model parameters	Symbol (unit)
Mechanical parameters	
Applied stress	σ (MPa)
Wire diameter	d (m)
Thermal exchange	
Ambient temperature	T_0 (K)
Electrical parameters	
Heating time	HT (s)
Cooling time	CT (s)
Maximum current	i (A)

6.1. Thermal effects

Fig. 8 shows the temperature and current curves during 2 actuation periods. The current values are similar between the experiment and modeling. It is expected since the current input in the model was set to be the same as for the experiment. The modeled temperature variation presents a good correlation with the experimental data, regarding the measured profile: first the Joule heating (represented by the fast temperature rise), then the thermomechanical coupling (represented by the 'plateau' sections in temperature) and the cooling by convection (represented by the exponential decrease of the temperature). Such evolution is as confirmation that the principal thermal phenomena were introduced in the model.

Nevertheless, a major disparity in temperature is observed at the end of the cooling time. This difference can be associated with two main factors: the inaccurate convection coefficient value and the heterogeneous temperature distribution along the wire in the real case. Regarding the last factor, during other experiments, a difference of approximately 15 °C between the hottest and coolest points along the wire length was found. This highlights the fact that the temperature is not homogeneous along the wire. Since the acquired experimental temperature corresponds to the maximum value for the all wire long, it cannot reflect different thermal conditions along the wire.

This heterogeneity is also perceived in strain measurements (Fig. 9). The experimental value for strain varies slowly when compared with the model. Indeed, due to the temperature heterogeneity, the phase transformation in the experiment is triggered at different moments along the wire, therefore, the strain varies more gently when compared with the model, for which only one integration point is considered (a simplification for a homogeneous temperature distribution). Additionally, the temperature vs. strain curves in Fig. 10 confirm this

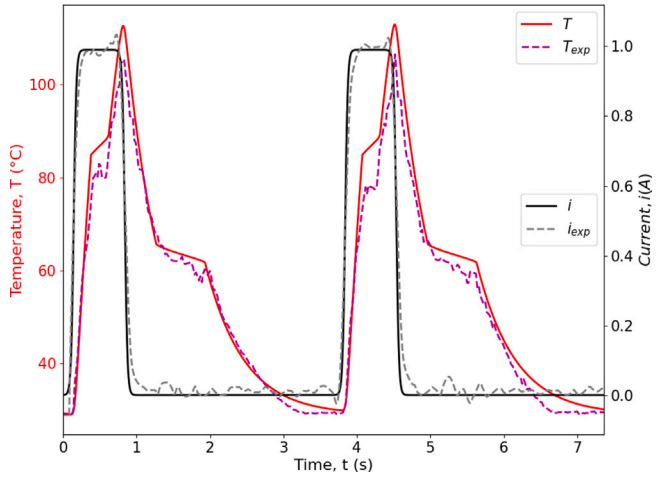

Fig. 8. Comparison between the simulated and the experimental results for the temperature and current response during two actuation time periods. The model curves are presented in plain lines and the experimental ones in dashed lines.

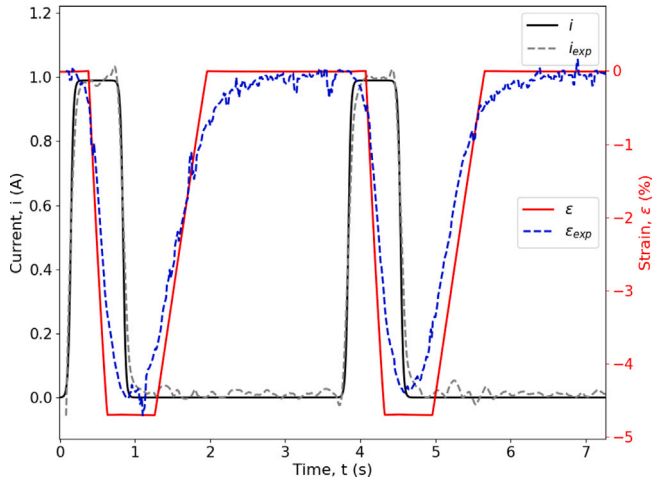

Fig. 9. Comparison between the simulated and the experimental results for the total strain and current response during two actuation time periods. The model curves are presented in plain lines and the experimental ones in dashed lines.

discrepancies source, despite the amount of total strain being well captured by the model.

In summary, the model demonstrates a good correlation with the experimental data. Some discrepancies were identified and they can be associated with the non-consideration of the SMA wire volume effects in the modeling. Nevertheless, as the model is to be implemented for cyclic conditions, adding volume effects would increase considerably the computation time. In the next section, the comparison between model and experiments in a cyclic context is addressed.

6.2. Cyclic effects

This latest comparison is performed in order to evaluate the modeling results during the long-term use of the actuator. For this analysis, the same experimental test as the one presented in the last section is used, except for the HT, now defined as 0.55 s. The cyclic model parameters (a_{tr}, b_{tr}) were evaluated from experimental tests and introduced in the model.

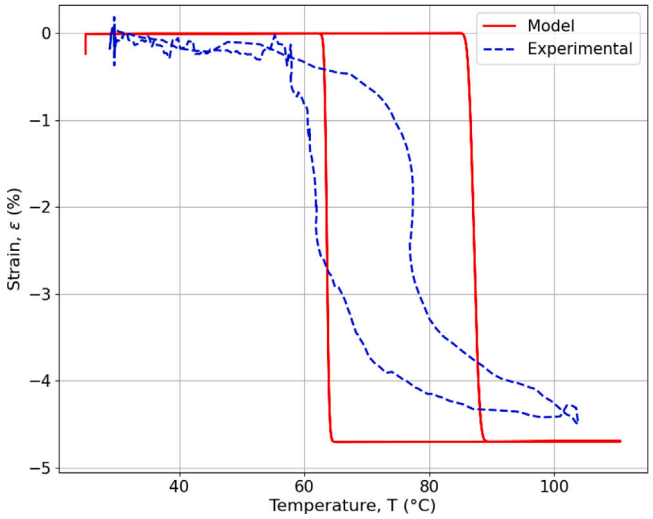

Fig. 10. Comparison between the simulated and the experimental results for the temperature vs. strain response during one actuation time period. The model curves are presented in plain lines and the experimental ones in dashed lines.

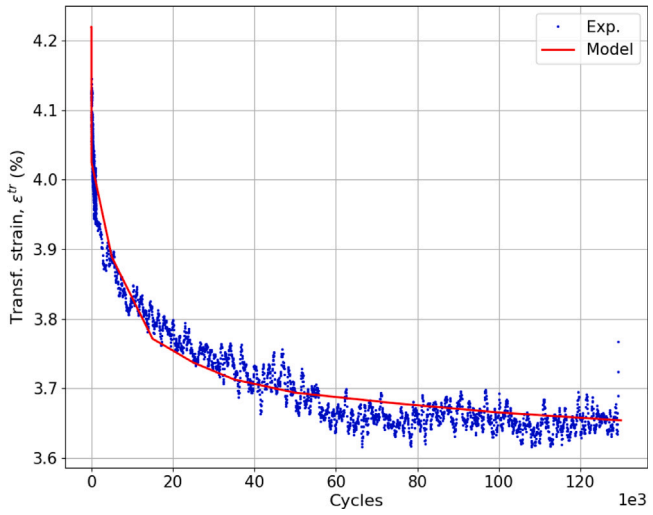

Fig. 11. Comparison between the simulated and the experimental results for the transformation strain degradation during 130k actuation cycles. The model curves are presented in plain lines and the experimental ones in dots.

It is worth mentioning that during the cyclic testing, the acquisition of the wire temperature was not performed. As the employed wire is very thin and the experiments are very long (about 8 days long), the use of thermocouples or infrared cameras did not reveal satisfactory. Therefore, the temperature comparison will not be addressed here. The comparison between experimental data and numerical simulations of parameters $ε^{r}$ and $ε^{tr}$ under FF loading are presented in Figs. 11–14.

Figs. 11 and 12, show that the degradation of the functional parameters $ε^{tr}$ and $ε^{r}$ are simulated with good accuracy by the proposed model. Fig. 14 shows that the model is capable of reproducing the shakedown state in an SMA actuator given its total number of thermal cycles.

Moreover, it can be noted that other cyclic mechanisms are also developed in the simulation. One of them is the change in the transformation temperature due to the internal stress accumulation [53], as can be seen in Fig. 14. Another is the mean temperature evolution of

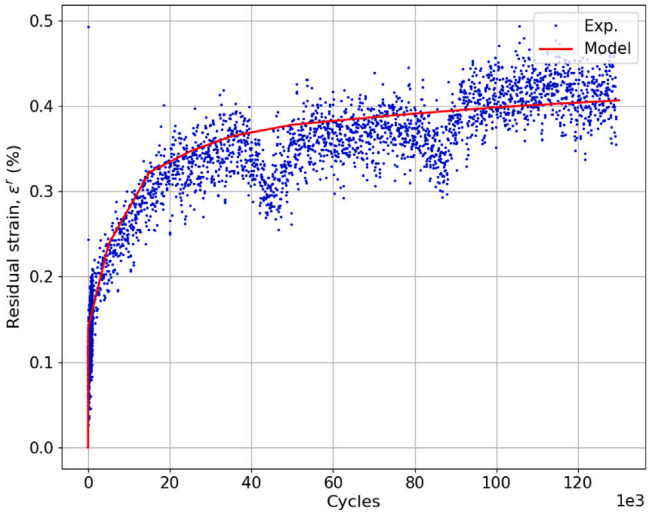

Fig. 12. Comparison between the simulated and the experimental results for the residual strain accumulation 130k actuation cycles. The model curves are presented in plain lines and the experimental ones in dots.

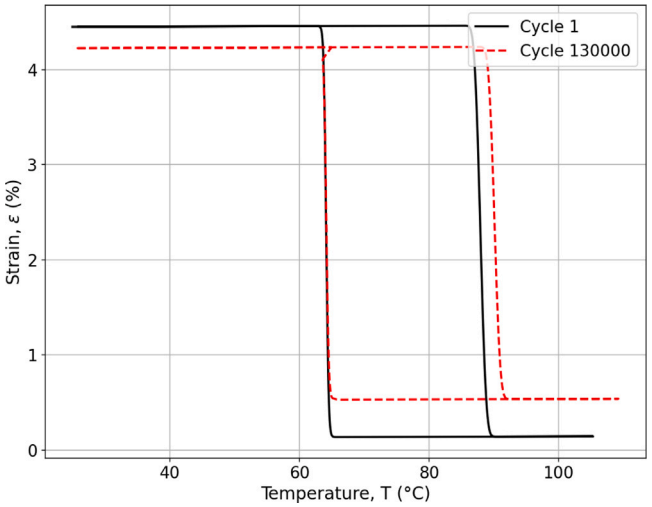

Fig. 13. Comparison between the first and the last simulated actuation cycles (130k) for the strain vs. temperature response. The first cycle behavior is presented in plain line and the last cycle behavior in dashed line.

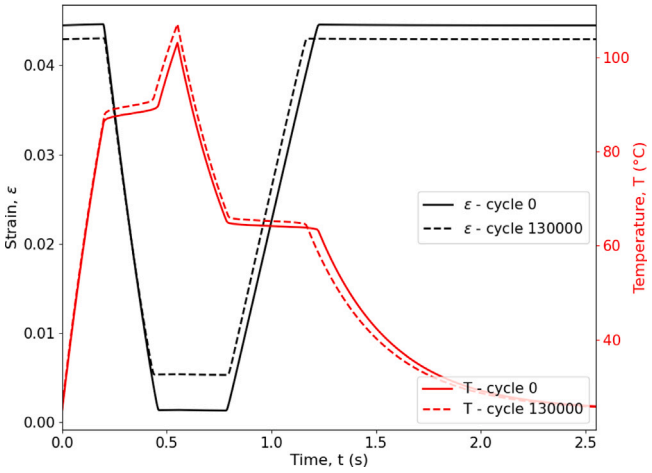

Fig. 14. Comparison between the first and the last simulated actuation cycles (130k) for the strain and temperature response during one actuation time period. The first cycle curves are presented in plain lines and the last cycle curves in dashed lines.

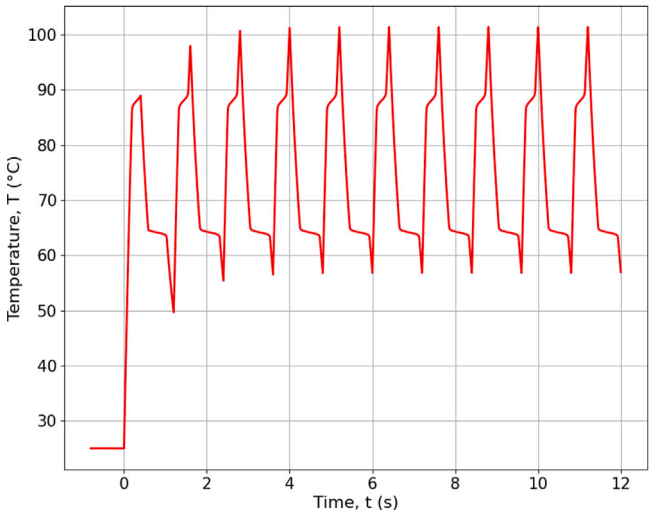

Fig. 15. Evolution of the average temperature during ten actuation time period at the conditions HT = 0.4 s, CT = 0.8 s and σ = 100 MPa.

the wire due to the rate dependence (thermomechanical coupling). The rate dependence is more evident in Fig. 15.

Conversely, some other aspects are also associated with the microstructure evolution of SMA during cyclic loading such as the reduction of the hysteresis area in the temperature vs. strain plot, the flattening of the phase transformation energy peaks (reduction of the latent heat amount for phase transformation) are not included in the model. These features could be further integrated into the model once the corresponding experimental data is available.

7. Conclusions

A constitutive model for SMA-based actuators exposed to long-term use (an industrial scenario) was developed. For the proposed modeling strategy, the most common actuation conditions were taken into account to propose a suitable simulation.

For the first time, a model links the Joule heating effect, the FF aspects, and the thermal exchange with surroundings to simulate the output of an SMA actuator during its lifetime including the degradation effects. For this purpose, well-known mechanisms active during cyclic loading such as dislocation accumulation and residual stress-induced martensite were first analyzed from experimental tests and inserted in the modeling strategy inspired by the original work of Lagoudas et al. [54]. Additionally, the thermomechanical interactions with the surroundings were introduced by the addition of thermomechanical coupling and heat exchange through the adequate heat equation.

The simulations of the implemented model in Python language were compared with experimental data and a good correspondence was found. The model was shown to be capable of reproducing the thermal effects and the wire temperature evolution with good accuracy and the FF with precision. In addition, an important feature, the thermomechanical coupling resulting from the phase transformation was also faithfully replicated in simulations, which ensured a greater precision on the obtained results. Nevertheless, some modeling aspects can be improved. To account for volume effects, a finite element strategy could be implemented to reproduce the thermal profile along the wire length. Furthermore, other material properties such as latent heat could be incorporated into the model for a finer adjustment of the simulation.

Overall, the presented modeling provides a useful framework for simulating and designing SMA actuators considering their whole lifespan and the different phenomena involved in their actuation.

CRediT authorship contribution statement

Marcos Lopes Leal Júnior: Conceptualization, Investigation, Data curation, Methodology, Validation, Writing – original draft. **Laurent Pino:** Investigation, Data curation. **Mahmoud Barati:** Conceptualization, Writing – review. **Luc Saint-Sulpice:** Conceptualization. **Laurent Daniel:** Supervision, Writing – review. **Shabnam Arbab Chirani:** Supervision, Conceptualization, Writing – review.

Declaration of competing interest

The authors declare the following financial interests/personal relationships which may be considered as potential competing interests: Laurent Daniel reports a relationship with FORVIA that includes: funding grants.

Data availability

Data will be made available on request.

Acknowledgment

The study was supported by the European Commission through the CPER EcoSysMer Eu000048 project.

Appendix. Material parameters identification

The aim of this section is to present readers the adopted methodology to identify the material parameters used on the validation of the proposed model. First, phase transformation temperatures Ms, Mf, As, Af, Rs and Rf of the implemented wire were determined by differential scanning calorimetry (DSC). The results are shown in Fig. A.16.

This initial test allowed defining the testing condition for pseudo-plastic (PP), superelastic (SE) and ASME loading paths. These tests were performed using a Zwick electromechanical testing machine (Zwick Z050) equipped with an extensometer to measure the axial strain, with a thermal chamber (Zwick BW91250) to control the temperature T surrounding the specimen and with a 500 N load cell to determine the axial stress σ.

For the ASME loading, a temperature rate of $\pm$ 4 °C/min was used. Whereas for the PP and SE loads, a low strain rate of $10^{-4}/s$ was imposed. For all tests, the wire temperature was measured by a K-type thermocouple. Additionally, for the ASME tests, the electrical resistivity

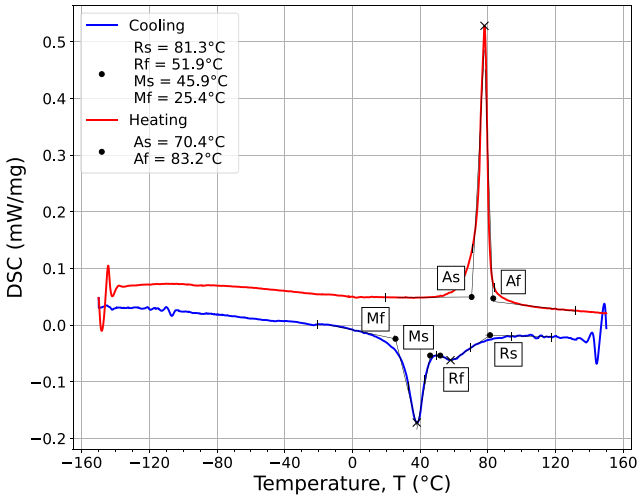

Fig. A.16. Results of the DSC tests for the studied wire. The identified transformation temperatures values are presented in the captions.

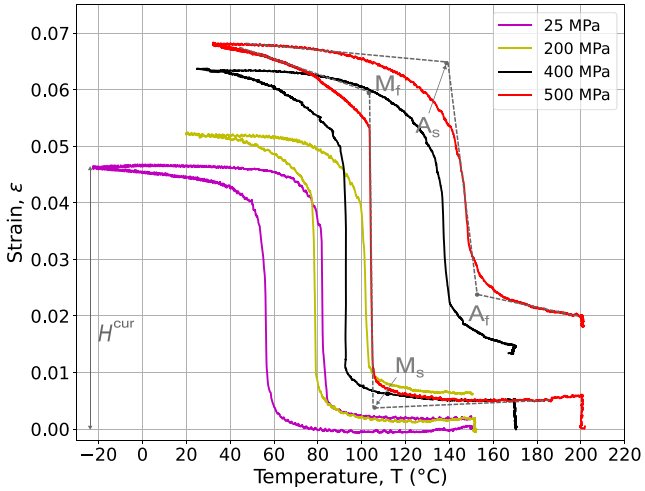

Fig. A.17. Strain-temperature response under ASME loads for studied. The maximum transformation strain (H^{cur}), transformation temperatures (M_s^σ, M_f^σ, A_s^σ and A_f^σ) amounts are represented in the graphics.

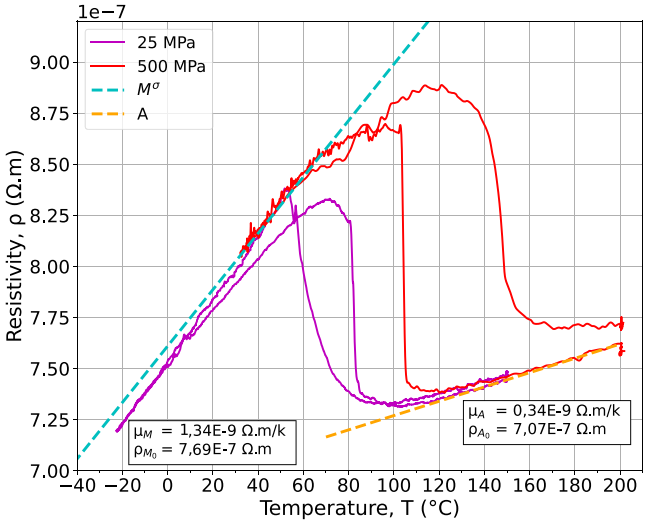

Fig. A.18. Resistivity diagram. The plain curves represent resistivity response under temperature variation for the two loading paths at 25 MPa and 500 MPa. The dashed lines denote the resistivity vs. temperature response for the austenite and the stress-induced martensite pure states. The corresponding parameters of the line equation are given in the captions.

was evaluated through a four-wire lead measurement method (see [8] for additional details about the adopted methodology).

The obtained results of the ASME loading are presented in two figures (Figs. A.17 and A.18). Fig. A.17 presents the thermomechanical response at four different load levels, while Fig. A.18 presents the electrical response. The latter is also known as resistivity diagram, and it presents the evolution of the characteristic electrical resistivity under temperature variation. The linear stages (dashed lines) correspond to an almost pure state of stress-induced martensite or austenite. From these line segments it is possible to obtain the following parameters μ_A, μ_M, ρ_A and ρ_M.

The phase transformation temperature at the adopted stress levels can also be collected from the ASME test. From this data, a phase diagram can be established. The same is presented in Fig. A.19.

The thermoelastic parameters E^A, E^M were obtained from PP and SE tests. The experimental results are presented in Figs. A.20 and A.21.

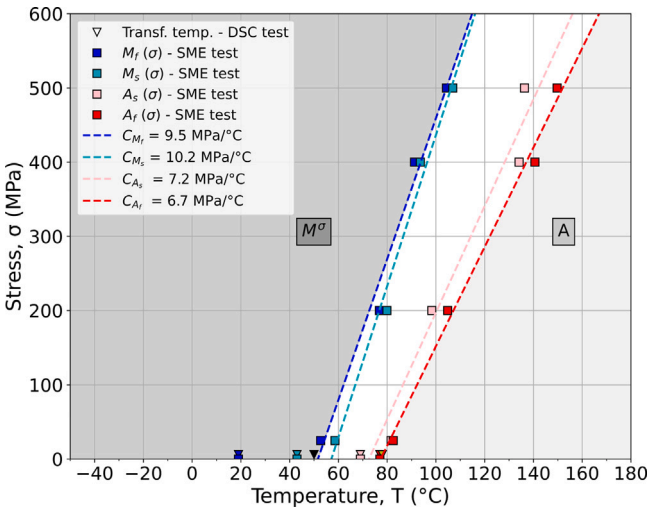

Fig. A.19. Phase diagram. The square markers represent the experimental points evaluated from the AMSE test. The triangle markers represent the experimental points evaluated from the DSC test. The dashed lines denote stress-temperature slopes for the initiation and termination of the phase transformation. The corresponding parameters of the slopes are given in the captions. The mean E_A value is given in the caption.

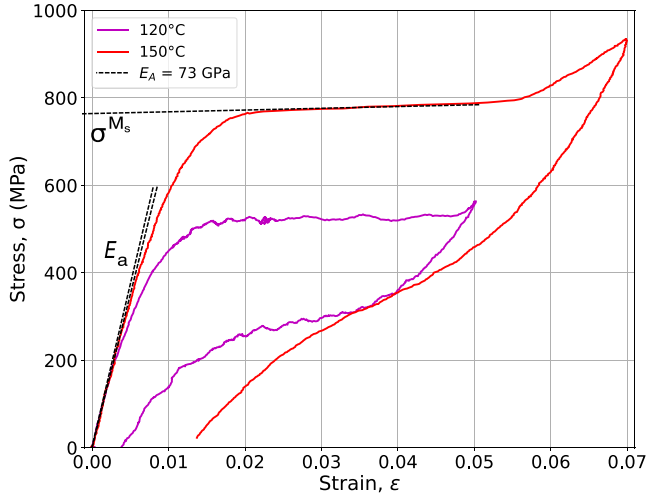

Fig. A.20. Stress–strain response under SE loads for studied wire. The initiation stress for forward transformation (σ^{M_s}), elastic modulus of the austenite phase (E_A) are represented in the graphics.

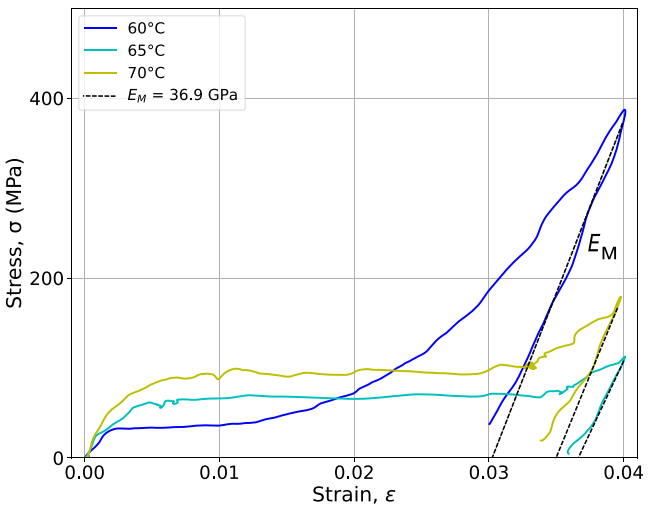

Fig. A.21. Stress–strain response under SE loads for studied wire. The elastic moduli of the martensitic phase (E_M) are represented in the graphics. The mean E_M value is given in the caption.

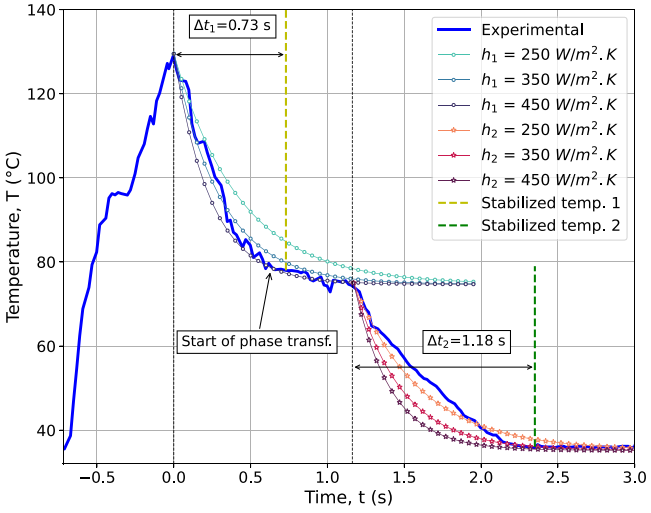

Fig. A.22. Illustration of the convection coefficient identification from a cooling curve. The plain curve represents the experimental temperature vs. time response. The bluish curves with the circle markers denote the fitting attempts before the phase transformation while the reddish curves with stars markers denote the fitting attempts after the phase transformation. The convection coefficients used at each fitting attempt are given in the caption.

For each loading path, the Young's modulus was evaluated by average from different testing temperatures.

Finally, the convection coefficient (h) was identified from a cooling curve of a given experimental test shown in Fig. A.22. This coefficient was evaluated in two different stages where the major thermal exchange was done by forced cooling only (without phase transformation). The first stage is between the hottest temperature and the start of the forward phase transformation and the second is between the end of the phase transformation and the ambient temperature. The coefficients were numbered as 1 and 2, respectively.

By comparing the different cooling curves at three levels of h it is possible to note that the value of 350 W/m^{2}k was the best-suited value for both cooling stages. Therefore, this is the adopted amount for this parameter.

References

[1] Kumar P, Lagoudas D. Introduction to shape memory alloys. In: Shape memory alloys: Modeling and engineering applications. Boston, MA: Springer US; 2008, p. 1–51. http://dx.doi.org/10.1007/978-0-387-47685-8_1.

[2] Ghosh P, Rao A, Srinivasa AR. Design of multi-state and smart-bias components using shape memory alloy and shape memory polymer composites. Mater Des 2013;44:164–71. http://dx.doi.org/10.1016/j.matdes.2012.05.063, URL https://www.sciencedirect.com/science/article/pii/S0261306912003731.

[3] Jani JM, Leary M, Subic A. Shape memory alloys in automotive applications. 2014, http://dx.doi.org/10.4028/www.scientific.net/AMM.663.248, URL https://www.scientific.net/AMM.663.248.

[4] Mertmann M, Vergani G. Design and application of shape memory actuators. Eur Phys J Spec Top 2008;158:221–30. http://dx.doi.org/10.1140/epjst/e2008-00679-9.

[5] Šittner P, Sedlák P, Seiner H, Sedmák P, Pilch J, Delville R, et al. On the coupling between martensitic transformation and plasticity in NiTi: Experiments and continuum based modelling. Prog Mater Sci 2018;98:249–98. http://dx.doi.org/10.1016/j.pmatsci.2018.07.003, URL https://www.sciencedirect.com/science/article/pii/S0079642518300719.

[6] Bian X, Heller L, Kadeřávek L, Šittner P. In-situ synchrotron X-ray diffraction texture analysis of tensile deformation of nanocrystalline NiTi wire in martensite state. Appl Mater Today 2022;26:101378. http://dx.doi.org/10.1016/j.apmt.2022.101378, URL https://www.sciencedirect.com/science/article/pii/S2352940722000178.

[7] Iaparova E, Heller L, Tuc O, Sittner P. Thermally induced reorientation and plastic deformation of B19' monoclinic martensite in nanocrystalline NiTi wires. Acta Mater 2023;242:118477. http://dx.doi.org/10.1016/j.actamat.2022.118477, URL https://www.sciencedirect.com/science/article/pii/S1359645422008540, publisher: Pergamon.

[8] Júnior MLL, Pino L, Barati M, Saint-Sulpice L, Daniel L, Chirani SA. Electric resistivity evolution in NiTi alloys under thermomechanical loading: phase proportioning, elasticity and plasticity effects. Smart Mater Struct 2023;32:065002. http://dx.doi.org/10.1088/1361-665X/accb21, publisher: IOP Publishing.

[9] Zaki W, Moumni Z. A 3D model of the cyclic thermomechanical behavior of shape memory alloys. J Mech Phys Solids 2007;55:2427–54. http://dx.doi.org/10.1016/j.jmps.2007.03.011, URL https://www.sciencedirect.com/science/article/pii/S0022509607000750.

[10] Delville R, Malard B, Pilch J, Sittner P, Schryvers D. Transmission electron microscopy investigation of dislocation slip during superelastic cycling of Ni–Ti wires. Int J Plast 2011;27:282–97. http://dx.doi.org/10.1016/j.ijplas.2010.05.005, URL https://www.sciencedirect.com/science/article/pii/S0749641910000707.

[11] Sedmák P, Šittner P, Pilch J, Curfs C. Instability of cyclic superelastic deformation of NiTi investigated by synchrotron X-ray diffraction. Acta Mater 2015;94:257–70. http://dx.doi.org/10.1016/j.actamat.2015.04.039, URL https://www.sciencedirect.com/science/article/pii/S1359645415002918.

[12] Huang K, Yin H, Li M, Sun Q. Grain size dependence of stress-assisted two-way memory effect in Ti-50.04 at.% Ni shape memory alloy. Mater Sci Eng A 2022;856:143872. http://dx.doi.org/10.1016/j.msea.2022.143872, URL https://www.sciencedirect.com/science/article/pii/S0921509322012527.

[13] Zhang Y, Chai X, Ju X, You Y, Zhang S, Zheng L, et al. Concentration of transformation-induced plasticity in pseudoelastic NiTi shape memory alloys: Insight from austenite–martensite interface instability. Int J Plast 2023;160:103481. http://dx.doi.org/10.1016/j.ijplas.2022.103481, URL https://www.sciencedirect.com/science/article/pii/S0749641922002583.

[14] Bo Z, Lagoudas DC. Thermomechanical modeling of polycrystalline SMAs under cyclic loading, Part III: evolution of plastic strains and two-way shape memory effect. Internat J Engrg Sci 1999;37:1175–203. http://dx.doi.org/10.1016/S0020-7225(98)00115-3, URL https://www.sciencedirect.com/science/article/pii/S0020722598001153.

[15] Dornelas VM, Oliveira SA, Savi MA. A macroscopic description of shape memory alloy functional fatigue. Int J Mech Sci 2020;170:105345. http://dx.doi.org/10.1016/j.ijmecsci.2019.105345, URL https://www.sciencedirect.com/science/article/pii/S0020740319330644.

[16] Lagoudas DC, Entchev PB. Modeling of transformation-induced plasticity and its effect on the behavior of porous shape memory alloys, Part I: constitutive model for fully dense SMAs. Mech Mater 2004;36:865–92. http://dx.doi.org/10.1016/j.mechmat.2003.08.006, URL https://www.sciencedirect.com/science/article/pii/S0167663603001194.

[17] Saint-Sulpice L, Chirani SA, Calloch S. A 3D super-elastic model for shape memory alloys taking into account progressive strain under cyclic loadings. Mech Mater 2009;41:12–26. http://dx.doi.org/10.1016/j.mechmat.2008.07.004, URL https://www.sciencedirect.com/science/article/pii/S0167663608001051.

[18] Morin C, Moumni Z, Zaki W. A constitutive model for shape memory alloys accounting for thermomechanical coupling. Int J Plast 2011a;27:748–67. http://dx.doi.org/10.1016/j.ijplas.2010.09.005, URL https://www.sciencedirect.com/science/article/pii/S0749641910001312.

[19] Yu C, Kang G, Kan Q, Zhu Y. Rate-dependent cyclic deformation of superelastic NiTi shape memory alloy, :Thermo-mechanical coupled and physical mechanism-based constitutive model. Int J Plast 2015;72:60–90. http://dx.doi.org/10.1016/j.ijplas.2015.05.011, URL https://www.sciencedirect.com/science/article/pii/S0749641915000819.

[20] Barrera N, Biscari P, Urbano MF. Macroscopic modeling of functional fatigue in shape memory alloys. Eur J Mech A Solids 2014;45:101–9. http://dx.doi.org/10.1016/j.euromechsol.2013.11.015, URL https://www.sciencedirect.com/science/article/pii/S0997753813001502.

[21] Chemisky Y, Chatzigeorgiou G, Kumar P, Lagoudas DC. A constitutive model for cyclic actuation of high-temperature shape memory alloys. Mech Mater 2014;68:120–36. http://dx.doi.org/10.1016/j.mechmat.2013.07.020, URL https://www.sciencedirect.com/science/article/pii/S0167663613001518.

[22] Chemisky Y, Hartl DJ, Meraghni F. Three-dimensional constitutive model for structural and functional fatigue of shape memory alloy actuators. Int J Fatigue 2018;112:263–78. http://dx.doi.org/10.1016/j.ijfatigue.2018.03.016, URL https://www.sciencedirect.com/science/article/pii/S0142112318301002.

[23] Zhu S, Zhang Y. A thermomechanical constitutive model for superelastic SMA wire with strain-rate dependence, smart. Mater Struct 2007;16:1696–707. http://dx.doi.org/10.1088/0964-1726/16/5/023, publisher: IOP Publishing.

[24] Wang J, Moumni Z, Zhang W. A thermomechanically coupled finite-strain constitutive model for cyclic pseudoelasticity of polycrystalline shape memory alloys. Int J Plast 2017;97:194–221. http://dx.doi.org/10.1016/j.ijplas.2017.06.003, URL https://www.sciencedirect.com/science/article/pii/S074964191730178X.

[25] Ju X, Moumni Z, Zhang Y, Zhang F, Zhu J, Chen Z, et al. A multi-physics, multi-scale and finite strain crystal plasticity-based model for pseudoelastic NiTi shape memory alloy. Int J Plasticity 2022;148:103146. http://dx.doi.org/10.1016/j.ijplas.2021.103146, URL https://www.sciencedirect.com/science/article/pii/S0749641921002138.

[26] Talebi H, Golestanian H, Zakerzadeh M, Homaei H. Thermoelectric heat transfer modeling of shape memory alloy actuators. 2014.

[27] Shayanfard P, Kadkhodaei M, Jalalpour A. Numerical and experimental investigation on electro-thermo-mechanical behavior of NiTi shape memory alloy wires. Iran J Sci Technol Trans Mech Eng 2019;43:621–9. http://dx.doi.org/10.1007/s40997-018-0183-8.

[28] Bouvet C, Calloch S, Lexcellent C. A phenomenological model for pseudoelasticity of shape memory alloys under multiaxial proportional and nonproportional loadings. Eur J Mech A Solids 2004;23:37–61. http://dx.doi.org/10.1016/j.euromechsol.2003.09.005, URL https://www.sciencedirect.com/science/article/pii/S0997753803001104.

[29] Auricchio F, Reali A, Stefanelli U. A macroscopic 1D model for shape memory alloys including asymmetric behaviors and transformation-dependent elastic properties. Comput Methods Appl Mech Engrg 2009;198:1631–7. http://dx.doi.org/10.1016/j.cma.2009.01.019, URL https://www.sciencedirect.com/science/article/pii/S0045782509000589.

[30] Morin C, Moumni Z, Zaki W. Thermomechanical coupling in shape memory alloys under cyclic loadings: Experimental analysis and constitutive modeling. Int J Plasticity 2011;27:1959–80. http://dx.doi.org/10.1016/j.ijplas.2011.05.005, URL https://www.sciencedirect.com/science/article/pii/S0749641911000817.

[31] Saint-Sulpice L, Arbab-Chirani S, Calloch S. Thermomechanical cyclic behavior modeling of Cu-Al-Be SMA materials and structures. Int J Solids Struct 2012;49:1088–102. http://dx.doi.org/10.1016/j.ijsolstr.2012.01.017, URL https://www.sciencedirect.com/science/article/pii/S0020768312000339.

[32] Lagoudas DC, Miller DA, Rong L, Kumar PK. Thermomechanical fatigue of shape memory alloys. Smart Mater Struct 2009;18:085021. http://dx.doi.org/10.1088/0964-1726/18/8/085021, publisher: IOP Publishing.

[33] Gao Y, Casalena L, Bowers ML, Noebe RD, Mills MJ, Wang Y. An origin of functional fatigue of shape memory alloys. Acta Mater 2017;126:389–400. http://dx.doi.org/10.1016/j.actamat.2017.01.001, URL https://www.sciencedirect.com/science/article/pii/S1359645417300010.

[34] Xu L, Solomou A, Baxevanis T, Lagoudas D. Finite strain constitutive modeling for shape memory alloys considering transformation-induced plasticity and two-way shape memory effect. Int J Solids Struct 2021;221:42–59. http://dx.doi.org/10.1016/j.ijsolstr.2020.03.009, URL https://linkinghub.elsevier.com/retrieve/pii/S0020768320300974.

[35] Owusu-Danquah JS, Saleeb AF. On the cyclic stability of the thermomechanical behavior of NiTi shape memory cylindrical actuators. Eur J Mech A Solids 2017;64:143–59. http://dx.doi.org/10.1016/j.euromechsol.2017.02.005, URL https://www.sciencedirect.com/science/article/pii/S0997753817301195.

[36] Scirè Mammano G, Dragoni E. Effect of stress, heating rate, and degree of transformation on the functional fatigue of Ni-Ti shape memory wires. J Mater Eng Perf 2015;24:2709–19. http://dx.doi.org/10.1007/s11665-015-1561-7.

[37] Alberto P, Savi M. An overview of constitutive models for shape memory alloys. Math Probl Eng 2006;2006. http://dx.doi.org/10.1155/MPE/2006/56876.

[38] Cisse C, Zaki W, Ben Zineb T. A review of constitutive models and modeling techniques for shape memory alloys. Int J Plast 2016;76:244–84. http://dx.doi.org/10.1016/j.ijplas.2015.08.006, URL https://www.sciencedirect.com/science/article/pii/S0749641915001436.

[39] Mirzaeifar R, Gall K, Zhu T, Yavari A, DesRoches R. Structural transformations in NiTi shape memory alloy nanowires. J Appl Phys 2014;115:194307. http://dx.doi.org/10.1063/1.4876715, URL https://aip.scitation.org/doi/abs/10.1063/1.4876715, publisher: American Institute of PhysicsAIP.

[40] Xu B, Kang G, Kan Q, Yu C, Xie X. Phase field simulation on the cyclic degeneration of one-way shape memory effect of NiTi shape memory alloy single crystal. Int J Mech Sci 2020;168:105303. http://dx.doi.org/10.1016/j.ijmecsci.2019.105303, URL https://www.sciencedirect.com/science/article/pii/S0020740319330164.

[41] Qidwai MA, Lagoudas DC. On thermomechanics and transformation surfaces of polycrystalline NiTi shape memory alloy material. Int J Plast 2000;16:1309–43. http://dx.doi.org/10.1016/S0749-6419(00)00012-7, URL https://www.sciencedirect.com/science/article/pii/S0749641900000127.

[42] Hartl DJ, Lagoudas DC, Calkins FT. Advanced methods for the analysis, design, and optimization of SMA-based aerostructures. Smart Mater Struct 2011;20:094006. http://dx.doi.org/10.1088/0964-1726/20/9/094006.

[43] Lagoudas D, Hartl D, Chemisky Y, Machado L, Popov P. Constitutive model for the numerical analysis of phase transformation in polycrystalline shape memory alloys. Int J Plasticity 2012;32-33:155–83. http://dx.doi.org/10.1016/j.ijplas.2011.10.009, URL https://www.sciencedirect.com/science/article/pii/S0749641911001793.

[44] Tabesh M, Lester B, Hartl D, Lagoudas D. Influence of the latent heat of transformation and thermomechanical coupling on the performance of shape memory alloy actuators. American Society of Mechanical Engineers Digital Collection; 2013, p. 237–48. http://dx.doi.org/10.1115/SMASIS2012-8188, URL https://asmedigitalcollection.asme.org/SMASIS/proceedings-abstract/SMASIS2012/45103/237/286492.

[45] Coleman BD, Noll W. The thermodynamics of elastic materials with heat conduction and viscosity. Arch Ration Mech Anal 1963;13:167–78. http://dx.doi.org/10.1007/BF01262690.

[46] Coleman BD. Thermodynamics of materials with memory. Arch Ration Mech Anal 1964;17:1–46. http://dx.doi.org/10.1007/BF00283864.

[47] Hartl DJ, Chatzigeorgiou G, Lagoudas DC. Three-dimensional modeling and numerical analysis of rate-dependent irrecoverable deformation in shape memory alloys. Int J Plast 2010;26:1485–507. http://dx.doi.org/10.1016/j.ijplas.2010.01.002, URL https://www.sciencedirect.com/science/article/pii/S0749641910000033.

[48] Yu C, Kang G, Kan Q, Xu X. Physical mechanism based crystal plasticity model of NiTi shape memory alloys addressing the thermo-mechanical cyclic degeneration of shape memory effect. Mech Mater 2017;112:1–17. http://dx.doi.org/10.1016/j.mechmat.2017.05.005, URL https://www.sciencedirect.com/science/article/pii/S0167663617302120.

[49] Makhloufi A, Aoues Y, El Hami A. 5 - Electro-thermo-mechanical modeling. In: El Hami A, Pougnet P, editors. Embedded mechatronic systems, vol. 2. Elsevier; 2015, p. 107–50. http://dx.doi.org/10.1016/B978-1-78548-014-0.50005-0, URL https://www.sciencedirect.com/science/article/pii/B9781785480140500050.

[50] DSof America. Coupled thermal-electrical analysis. 2017, URL https://abaqus-docs.mit.edu/2017/English/SIMACAEANLRefMap/simaanl-c-jouleheating.htm.

[51] Ortiz M, Simo JC. An analysis of a new class of integration algorithms for elasto-plastic constitutive relations. Internat J Numer Methods Engrg 1986;23:353–66. http://dx.doi.org/10.1002/nme.1620230303, _eprint: https://onlinelibrary.wiley.com/doi/pdf/10.1002/nme.1620230303, URL https://onlinelibrary.wiley.com/doi/abs/10.1002/nme.1620230303.

[52] Holm R. Electric contacts. Berlin, Heidelberg: Springer; 1967, http://dx.doi.org/10.1007/978-3-662-06688-1, URL http://link.springer.com/10.1007/978-3-662-06688-1.

[53] Kang G, Kan Q, Qian L, Liu Y. Ratchetting deformation of super-elastic and shape-memory NiTi alloys. Mech Mater 2009;41:139–53. http://dx.doi.org/10.1016/j.mechmat.2008.09.001, URL https://www.sciencedirect.com/science/article/pii/S0167663608001191.

[54] Lagoudas D, Li C, Miller D, Rong L. Thermomechanical transformation fatigue of SMA actuators. Proc SPIE - Int Soc Opt Eng 2000;60. http://dx.doi.org/10.1117/12.388225.